6-26-2015

A Hybrid Supercapacitor and Direct Borohydride Fuel Cell DC-DC Converter for Portable Applications

Matthew J. Tarca
University of Connecticut - Storrs, matt.tarca@gmail.com

A Hybrid Supercapacitor and Direct Borohydride Fuel Cell DC-DC Converter for Portable Applications

Matthew Tarca

B.Eng., University of Connecticut, 2009

A thesis

Submitted in Partial Fulfillment of the

Requirements for the Degree of

Masters of Science

At the

University of Connecticut

2015

APPROVAL PAGE

Masters of Science Thesis

A Hybrid Supercapacitor and Direct Borohydride Fuel Cell DC-DC Converter for Portable Applications

Presented by

Matthew Tarca, B.Eng.

Major Advisor_____
Sung-Yeul Park

Associate Advisor_____
Ugur Pasaogullari

Associate Advisor_____
Prabhakar Singh

University of Connecticut

2015

Acknowledgements

The author would like to thanks Dr. Ugur Pasaogullari and Dr. Prabhakar Singh for their pioneering research with direct-borohydride fuel cell that ultimately allowed me to pursue power electronics research around the fuel cell system. Their research was fundamental in characterization and understanding of the fuel cell that paved the way for further study and collaboration. Additionally, Dr. Yongsheen Hwang also had an important role with his additional contributions to fuel cell characterization. His contributions greatly advanced our understanding of mechanical and chemical fuel cell considerations. I would like to thank my colleagues, Xiao Zhu for beginning the fuel cell power electronics research this thesis is based on. Also, sincerest thanks to Dr. Tai-Sik Huang, Dr. Sungmin Park, and Yongduk Lee: because of your experience and generosity in teaching you were instrumental in my understanding of power electronics and I could not have created this work without your help. Finally, I would like to thank my advisor Professor Sung-Yeul Park for all of your guidance, support, and encouragement. I will always be grateful for everything you have done for me and the career path you help set me on. Thank you.

Table of Contents

List of Tables

List of Figures

Abstract

Access to electrical energy is of ever increasing importance in modern society. Devices that require portable power to operate while not connected to a typical grid continue to proliferate and there is a large scale search underway across academia and industry to find the best solutions for providing portable power. Fuel cells offer a great promise in both stand-alone and portable applications. The research presented herein regards a high energy-density fuel cell system paired with a power converter for portable applications. A class of fuel cells known as direct-borohydride fuel cells offer higher energy density than typical proton exchange membrane fuel cells fuel using hydrogen or hydrocarbon fuels. Both the steady state and dynamic electrical characteristics of this fuel cell are studied using V-I curve characterization and electrochemical impedance spectroscopy. To create a regulated, usable power supply, a non-isolated, synchronously switched DC/DC boost converter topology was selected. Using state-space averaging techniques, transfer functions for this converter are derived. With these transfer functions and the fuel cell characterization a custom control loop is designed. Additionally, the inclusion of an input supercapacitor is proven to improve converter transient response and is added to the model. The supercapacitor is also shown to have the added benefit of energy storage, eliminating the need for batteries or additional interface converters for remote startup. A prototype power converter was constructed and the final fuel cell system was tested under various load conditions and dynamics. The control algorithm was implemented digitally via a Texas Instruments TMS320F28035 processor.

Chapter 1: Introduction

1.1. Research Motivation

At present there is an increasing penetration of portable electronics and electronics technology that require high quality DC power for operation. As tablets, personal computers, cell phones, and electric vehicles (to name a few applications) continue to grow in popularity in the commercial sector while wearable power, reconnaissance drones, radio equipment, and other emerging technology increase in popularity in the military world. This trend will continue for the foreseeable future. In every portable application, energy density expressed as kWh/kg is a desirable metric in order to store as much energy as possible while carrying as little weight as possible. Furthermore, in some applications power density expressed as kW/kg becomes an important factor where constant levels of higher current and power or high levels of pulsed current and power are required. This research intends to provide a stable and robust portable power system that offers compelling energy density.

1.2. Fuel Cells and the Direct Borohydride Fuel Cell

Fuel cells are devices capable of creating electrical energy as the result of a chemical reaction that the fuel cell facilitates. Unlike batteries, fuel cells do not store chemical energy internally to be later converted into electrical energy; rather they are physical devices capable of sourcing electrical energy when fuel is supplied to and utilized by the fuel cell [1].

The physical properties of fuel cells were discovered by Sir William Grove in 1839 and had a configuration similar to that in Figure 1.1 [2]. The diagram of Figure 1.1a depicts water being electrolyzed into H_2 and O_2 due to an external battery inducing current through the circuit. However, the reverse of this process is Figure 1.1b where H_2 and O_2 recombine to form water and provide free electrons into an external circuit producing electric current. The chemical reaction can be summarized in (1.1).

$$2H_2 + O_2 \rightarrow 2H_2O \tag{1.1}$$

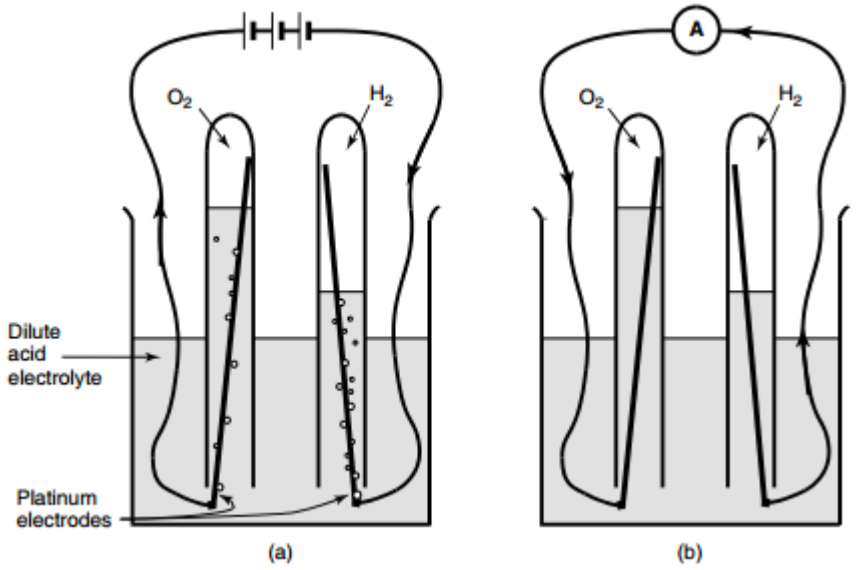

Figure 1.1. Electrolysis created by an external circuit (a) and its reverse, electrical current supplied externally due the reaction of hydrogen and oxygen as a fuel cell (b) [2].

Since this original fuel cell was developed the structure of fuel cells have been modified greatly to optimally produce electrical energy from supplied fuels and many varieties of fuel sources and fuel cell structure have been developed. Depending on the fuel cell structure, fuel composition, cost, etc. several fuel cell types have found niche

applications in energy production ranging from general purpose home and commercial generation, underwater, anaerobic high atmosphere and remote applications.

1.3. Fuel cell classifications

In Figure 1.1 water was simply used as the "electrolyte" through which H^+ ions passed through originating from the anode and recombining at the cathode with the freed electrons. Various types of electrolytes along with the anode and cathode fuels are what generally determine a fuel cells classification [2-4]. A summary of fuel cell types currently receiving the majority of research and commercialization attention can be seen in Table 1.

Table 1.1. Classification, ion type, standard operating temperature, and application examples of today's most common fuel cells. [2]

Fuel cell type	Mobile ion	Operating temperature	Applications and notes
Alkaline (AFC)	OH^-	50–200°C	Used in space vehicles, e.g. Apollo, Shuttle.
Proton exchange membrane (PEMFC)	H^+	30–100°C	Vehicles and mobile applications, and for lower power CHP systems
Direct methanol (DMFC)	H^+	20–90°C	Suitable for portable electronic systems of low power, running for long times
Phosphoric acid (PAFC)	H^+	~220°C	Large numbers of 200-kW CHP systems in use.
Molten carbonate (MCFC)	CO_3^{2-}	~650°C	Suitable for medium- to large-scale CHP systems, up to MW capacity
Solid oxide (SOFC)	O^{2-}	500–1000°C	Suitable for all sizes of CHP systems, 2 kW to multi-MW.

The proton exchange membrane fuel cell (PEMFC) in table 1.1 operates directly with hydrogen and oxygen as fuels. The direct methanol fuel cell (DMFC) is an extension of the PEMFC and is so called "direct" because it uses liquid methanol as opposed to first extracting hydrogen from the methanol. This nomenclature shares the same meaning with respect to the use of "direct" in "DBFC" since borohydride is directly used as fuel.

DMFC's have lower power density then PEMFC's but are still widely popular due to the availability of methanol and thus the fuel cells flexibility and availability of fuel source. They succeed in applications where power density is not a key requirement.

One difficulty in designing fuel cells is related to achieving the highest possible reaction rate of the fuel and oxidant within the fuel cell. Higher temperature and pressures increase reaction rates, otherwise typically more expensive and complicated catalysts such as platinum is required. Hence, from Table 1.1 molten carbonate and solid oxide fuel cells are typically capable of producing reactions with less expensive catalysts such as nickel while the remaining types require more expensive and complex methods. However, the higher temperature fuel cells still require costly ceramics and cooling and heating elements that significantly impact the cost of the fuel cell.

Alkaline fuel cells (AFCs) use highly porous electrodes, platinum catalysts and sometimes even high pressures to achieve sufficient reaction rates at lower temperatures. The main drawback of AFC's is that CO_2 must not be present in the fuels or pure hydrogen and oxygen must be used. However, this makes AFC's a viable option for space, and indeed AFC's were used on the Apollo and Shuttle Orbiter craft.

1.4. Applications of fuel cell

There have been a number of successful applications of fuel cells for decades. Interest in fuel cells continues to grow as industry continues to pursue cost reductions and efficiency improvements in fuel cell technology. Some of the applications of fuel cells are itemized below [5]:

(1) Automobiles: Most car manufactures have at least produced a prototype of a fuel cell vehicle (FCV), but the company currently leading by far is Toyota. The Toyota Mirai is slated to be available in late 2015 and be the first mass produced FCV. It will use stored hydrogen and oxygen (PEMFC) to power the vehicle while only producing water as a byproduct. Figure 1.2 shows the Toyota Mirai while Figure 1.3 shows a high level system block diagram of the fuel cell and electric propulsion system.

Figure 1.2. Toyota's PEMFC fuel-cell vehicle, the Mirai. Image courtesy of Toyota Motor Co., Inc.

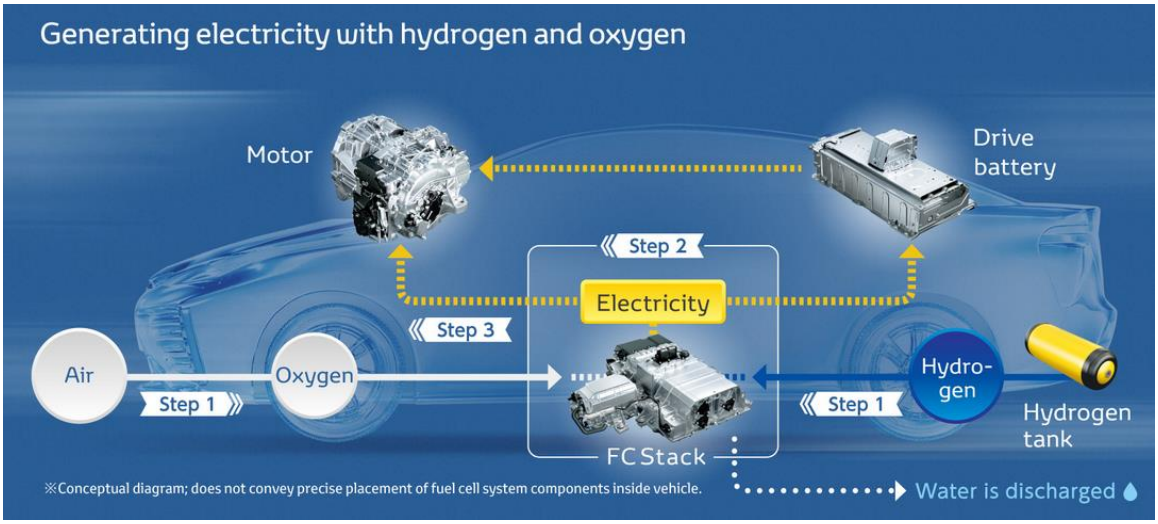

Figure 1.3. Toyota Mirai system block diagram. Image courtesy of Toyota Motor Co., Inc.

(2) Stationary applications: One of the leaders in stationary fuel cell systems is Fuel Cell Energy in Danbury, CT. They produce fuel calls ranging from 300kW to multi-megawatt scale systems. Their Direct FuelCell® (DFC®) power plants can utilize a variety of fuels including renewable biogas from wastewater treatment and food processing, as well as clean natural gas, directed biogas and propane. Bloom Energy is a company pursuing stationary, distributed generation with a proprietary solid-oxide fuel cell. They offer scalable 160-200kW cells that are scalable and claim to be cost effective due to low cost material construction, high efficiency, and fuel flexibility [6].

(3) Space and Sea: NASA was one of the pioneering organizations to use fuel cells. Gemini, Apollo, Centaur, and Shuttle spacecraft have all made use of alkaline fuel cell power systems for decades [7]. Further, many small aircraft and unmanned aerial vehicles (UAV's) have been demonstrated to fly running solely on fuel power alone, such as the modified Dimona air-glider aircraft demonstrated by Boeing [8]. The anaerobic nature and power density of certain fuel cell types has also made them good applicants for underwater stationary or mobile power supply systems. Protonex is a company employing a PEM-based fuel cell that uses sodium borohydride and hydrogen peroxide ($NaBH_4, H_2O_2$, the same fuel and oxidant used in this paper) to generate underwater power [9].

(4) Portable applications: There is interest in the opportunity to replace batteries with fuel cells in consumer electronics and other battery based systems. These systems face many challenges including fuel storage, reaction by-product storage, balance of plant, and fitting all of these components into a small enough mechanical

package. However, companies such as Horizon Fuel Cell have developed portable fuel cell technologies based on PEM fuel cell technologies allowing consumers to power their portable devices on the go using hydrogen and oxygen.

1.5. Design motivation of DBFC power conditioning system for portable applications

In portable applications, energy density is of key concern. DBFC's have a theoretical energy density greater than hydrogen based PEM fuel cells as well as Lithium Ion batteries [10]. Additionally, a DBFC can be operated at room temperature and in doing so removes the complexity and risks associated with higher temperature fuel cells. As previously described in [11] a DBFC stack has been researched and characterized by a group at the University of Connecticut's Center for Clean Energy Engineering. While a commercial off-the-shelf converter was originally to be included in the design, the purchased converters were found to be incapable of producing efficient and reliable output. Thus, a converter optimized for stability and small size is to be designed. The DBFC has a normal output voltage of 4-8 volts depending mostly on load conditions. The selected converter topology is a boost converter which will generate a regulated 12V output, something that can be used by a large range of portable electronics such as laptop computers.

Figure 1.4 shows the block diagram of the system.

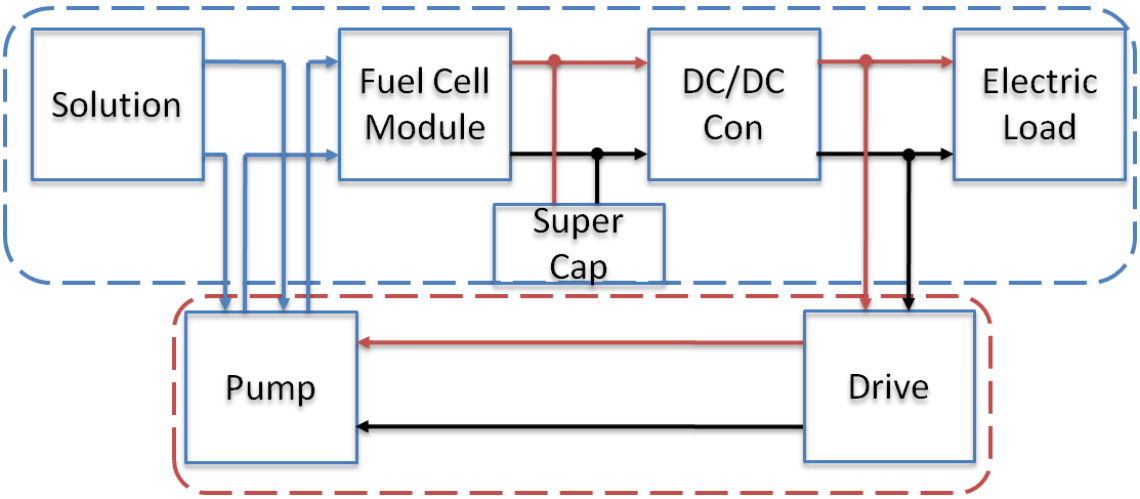

Figure 1.4. Block diagram of the DBFC boost converter system

1.6. Fundamentals of DBFC

Direct borohydride fuel cells are devices that convert chemical energy stored in borohydride ions ($BH4-$) and an additional oxidant directly into electricity by redox processes [10]. Sodium borohydride ($NaBH_4$) is used as the fuel and hydrogen peroxide as the oxidant, although oxygen is an alternative option. One of the key proposed advantage of the DBFC is its higher theoretical energy density of up to 9.3 kWh/kg compared to that of a methanol fuel cell at 6.1 kWh/kg [12]. Furthermore, 9.3 kWh/kg has an even larger advantage over modern day lithium ion batteries which have an energy density of 0.2 kWh/kg) [13]. In [14], it is shown that hydrogen peroxide and sodium borohydride at the electrodes produce more than a 30% higher voltage output compared to an ordinary hydrogen or oxygen PEMFC. Other advantages of the DBFC include air-independent operation and simplified fuel storage [15].

Generating an equivalent circuit model of the DBFC will allow for the design of custom power converter optimized to work with the DBFC. Various equivalent circuit

models have been proposed [16-18]. These models focus mostly on the internal electro-chemical reactions. This paper is more concerned with an electrical equivalent model and thus has developed one using electrochemical impedance spectroscopy (EIS) with a frequency response analyzer (FRA) [19]. As will be seen, for a large number of applications the electrical model of a fuel cell can be simplified to a simple voltage source with equivalent series resistance.

1.7. Power conversion system

Power conditioning systems are a subset of the study of power electronics. They can be summarized as electrical circuits that can translate any combination of DC or AC voltages and currents to some other form of DC or AC voltage or current as well as those that simply 'condition' power such as active power filters. The classes of converters include DC/DC converter, DC/AC inverter, AC/DC rectifier, and AC/AC cyclo-converter. Many systems include several of these types of converters to create a system. For example, typical electronics chargers that are ubiquitous today first convert the AC voltage available in typical wall outlets from 120 AC volts to a regulated DC voltage (often 12V) using a rectifier or more advanced power-factor correction circuit. Then, depending on the electronic device, various levels of DC voltage or current are needed, so further DC/DC converters are utilized that draw power from a 12V bus and create the necessary outputs. These outputs may be 5V, 3.3V, 1.8V, etc. An example similar to this is shown in Figure 1.5. This circuit uses the more efficient approach to rectification than a simple rectifier bridge called a power-factor correction AC/DC converter. This creates a regulated

DC voltage at the node labeled “VBUS”. The second portion of the circuit uses a quasi-resonant half-bridge stage to create another regulated DC voltage output driving LEDs.

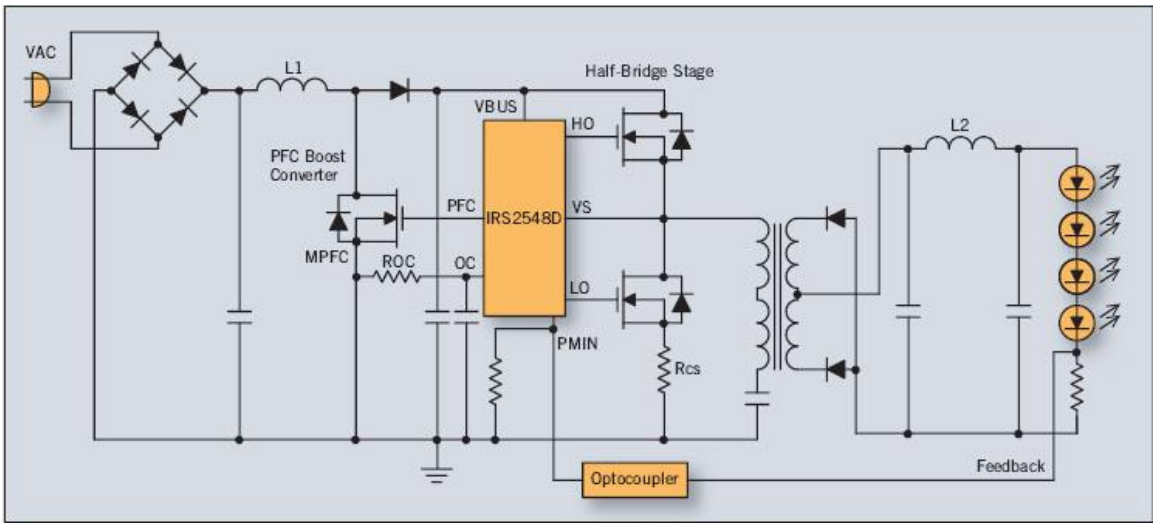

Figure 1.5. An example power electronics converter utilizing an AC/DC and DC/DC converters to efficiently drive LED lighting with 120V commercial/residential utility power. Image courtesy of PowerElectronics.com.

In the case of the DBFC, a simpler circuit can be used. The DBFC produces an output voltage proportional to many environmental conditions. The environmental condition with the greatest impacts are the load, fuel flow rate and composition, and temperature. Since optimal fuel flow rates have already been studied by other groups at the University of Connecticut, this fuel composition will be used. Further, all tests that utilize the fuel cell will be run in a room temperature atmosphere and will allow for the DBFC to reach an operating equilibrium temperature before proceeding. Thus, for the purposes of designing a power electronics converter only the load conditions will be considered. Across the load ranges of interest, the DBFC will produce an output voltage in the range of [4~8] volts. Since it is desired to create a regulated 12 volt output this

situation requires only a single power electronics stage: a DC/DC converter. Because the output voltage of the DC/DC converter will always be greater than the input this particular class of converters is known as “boost” (as opposed to “buck” or “buck-boost”). Since the power rating of this system is low (<100W), a basic non-isolated boost topology was selected. Efficiency is also of high concern and choosing an isolation-less system also has the advantage of avoiding any losses that would have been incurred in a transformer. Also in an attempt to improve efficiency the diode normally used in this topology is replaced with an additional MOSFET switch allowing for a boost converter operating in a configuration known as “synchronously switched.” This also introduces an interesting symmetry because once the diode has been replaced with a switch it is possible to use the converter in the “opposite” direction as a non-isolated buck converter. This will become useful later when discussing the charging an input supercapacitor.

Next, in this topology it is possible to add additional boost converter “legs” consisting of an additional inductor and switches/diodes, thus creating what is known as an interleaved boost converter. If the boost converter is interleaved with two legs and the duty cycle of the converter is 50% there is theoretically zero input current ripple, potentially advantageous to maximum utilization of the DBFC in terms of efficiency. Ultimately, the converter and its surrounding components can be seen in Figure 1.6.

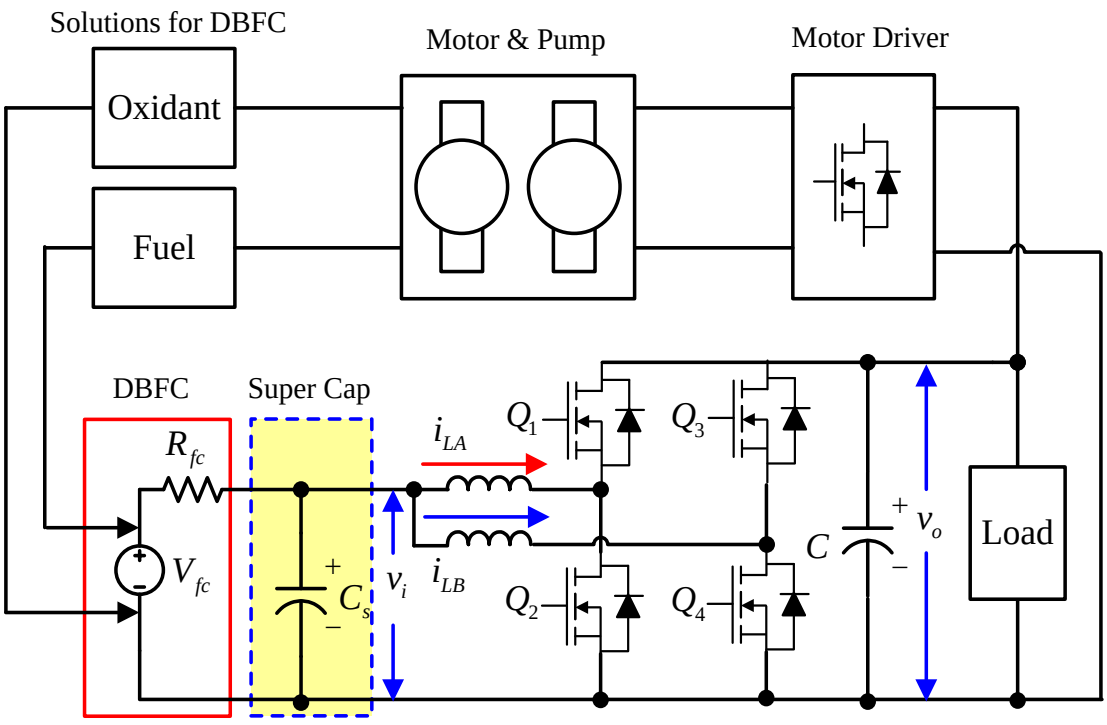

Figure 1.6. An interleaved, synchronously switched boost converter. The circuit also includes the fuel cell source voltage V_{fc} and its series resistance R_{fc}, an input supercapacitor C_s, an output capacitor C and a load. The other components illustrate how fuel will physically be supplied to the fuel cell.

The basic transfer functions of such a circuit are well studied and understood making control design of the system simpler. Not shown in Figure 1.6 is a simple voltage divider and op-amp low pass filter conditioning circuit used for sensing the output voltage used in the final voltage mode control algorithm. Using this circuitry a plant model in the s-domain has been developed and used to develop a robust and responsive voltage mode controller. This power conditioning system was shown to be able to create a well regulated 12V output with a variety of loads and input voltages ranging from 4 volts to 8 volts.

Chapter 2: Characteristics of a DBFC

One of the key requirements for developing an optimal power electronics converter regulating the DBFC voltage is to a have a good electrical understanding of the DBFC as a source. This chapter introduces more detail about the operating principles of the DBFC, creating an electrical model of the DBFC and ultimately simplifying that model to one that is easier to work with yet still captures the basic dynamics and voltage-current characteristics of the DBFC.

2.1. Electrochemistry of the DBFC

As previously described, a fuel cell consists of anode and cathode sides that accept various fuels which react across a layer of electrolytes that allows freed electrons to flow in an externally connected circuit. In the case of the DBFC under consideration the fuels are sodium borohydride $NaBH_4$ in a solution of sodium hydroxide $NaOH$ and a hydrogen peroxide H_2O_2 sulfuric acid H_2SO_4 mixture. The outputs of the fuel cell are water and sodium boroxide $NaBO_2$. Oxygen can also be used in place of peroxide, but peroxide allows for a stable liquid solution as well as air-independent operation. The electrochemical reactions of the DBFC take place under an alkaline medium because borohydride ions are not chemically stable in acidic media [11]. Figure 2.1 depicts the chemical reaction that yields 8 free electrons within the DBFC. Of note is that fact that positively charged sodium ions act as the charge carriers as opposed to the common positively charged hydrogen ion in most PEM fuel cells. There are several concerns about

these types of fuel cells ranging from electrolyte membrane type, mass transport losses and recombination losses that are well described in [20].

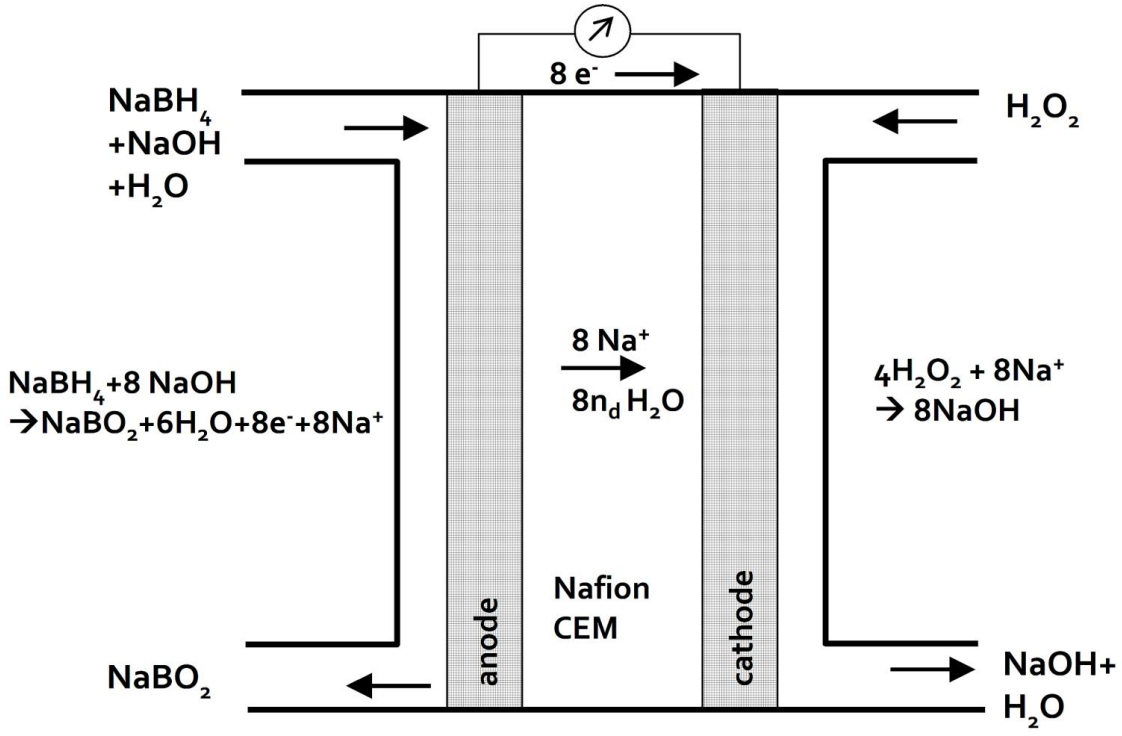

Figure 2.1. Fuel, oxidant, electrochemical reactions and ultimate reactant outputs

2.2. V-I curve of DBFC

First, the 5-cell DBFC available was characterized at a very fundamental voltage-current characteristic level to obtain a baseline V-I curve. Fuel cells exhibit a particular V-I characteristic that is related to the chemical reactions occurring within. Figure 2.2 shows a general fuel cell V-I curve showing the three main regions: active polarization region, ohmic region, and concentration polarization region. These three regions can be considered as the three major contributing sources of loss in a fuel cell. Firstly at low current densities the activation polarization losses begin due to sluggish kinetics of the chemical reactions, then at intermediate current densities the ohmic polarization region

occurs due to ohmic losses in the external circuit as well as resistance to positively charge ions moving through the electrolyte, and finally at high current densities the area of concentration polarization with mass transport losses dominate due to the transport limit of the reactant through the pore structure of the GDL and electro catalyst layers [21]

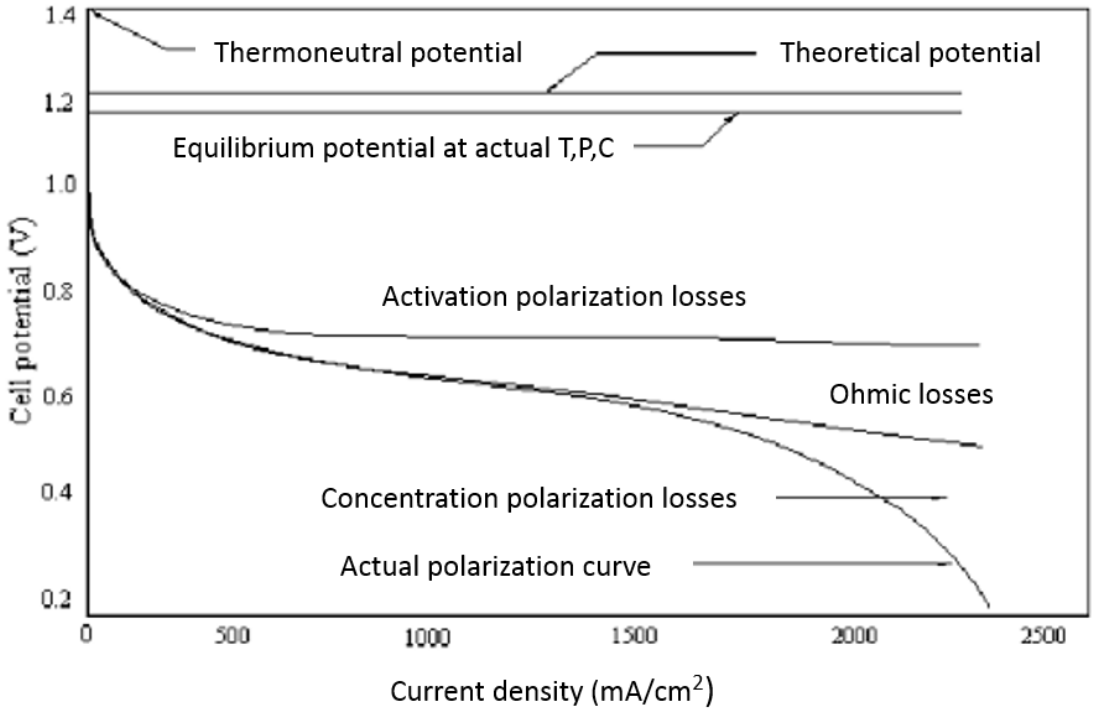

Figure 2.2. Fuel cell V-I characteristic regions [21]

A programmable electrical load (Amrel FEL 60-1) was used to obtain the V-I results shown in Figure 2.3. This Figure also shows the V-I characteristics for various pump flow rates whose mL/min is specified in table 2.1. The activation, ohmic, and concentration regions can be roughly seen as well as the fact that the cell voltage ranged from roughly 4-8 volts while producing current in the range of 0 to 10 Amps. The data points for the voltage versus current for each flow rate test are separately shown in Figure 2.4 and the

corresponding power curves are shown in Figure 2.5. Aside from the initial activation polarization region it can be observed that fuel can almost entirely be described via ohmic losses.

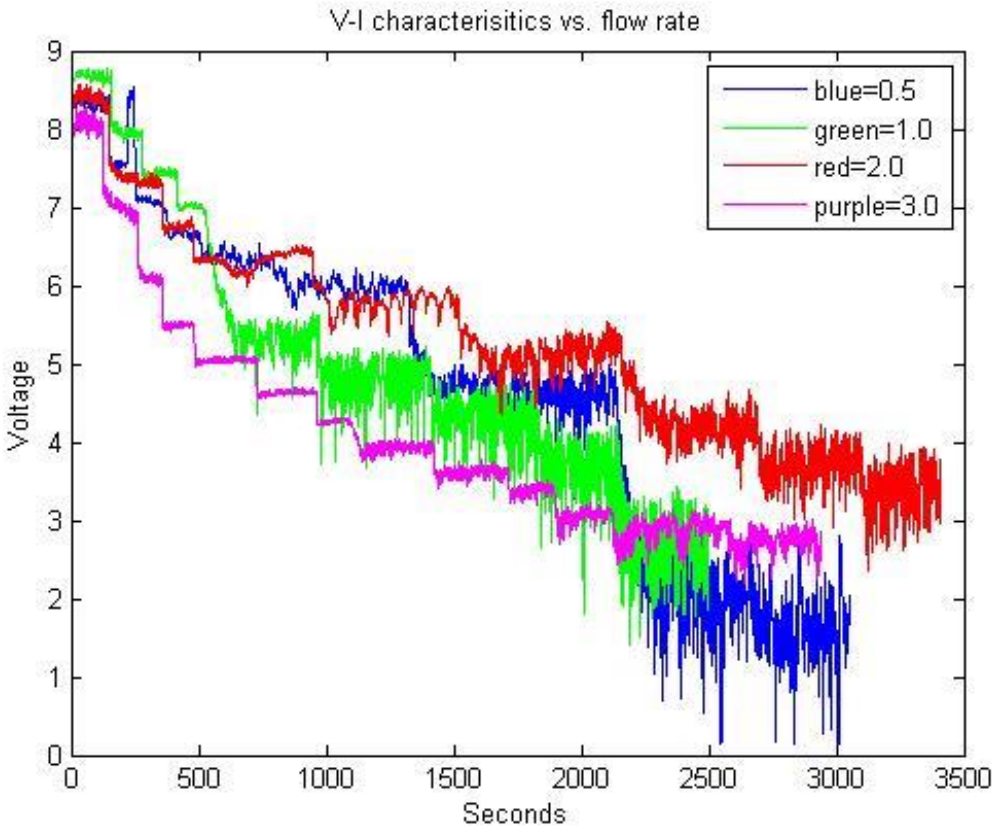

Figure 2.3. Experimentally found V-I characteristics for varying flow rates.

Table 2.1. VI test pump speeds.

Pump Setting	Physical meaning
0.5	4.7733 mL/min
1	8.3877 mL/min
2	16.7785 mL/min
3	26.2238 mL/min

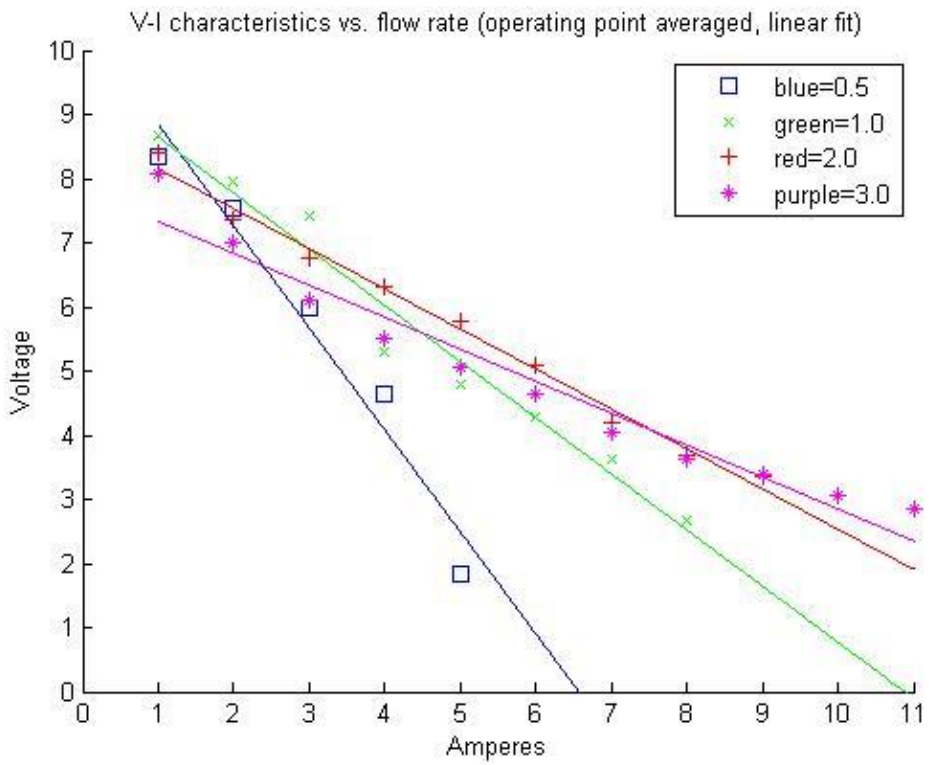

Figure 2.4. V-I characteristics vs. flow rate, linear fit.

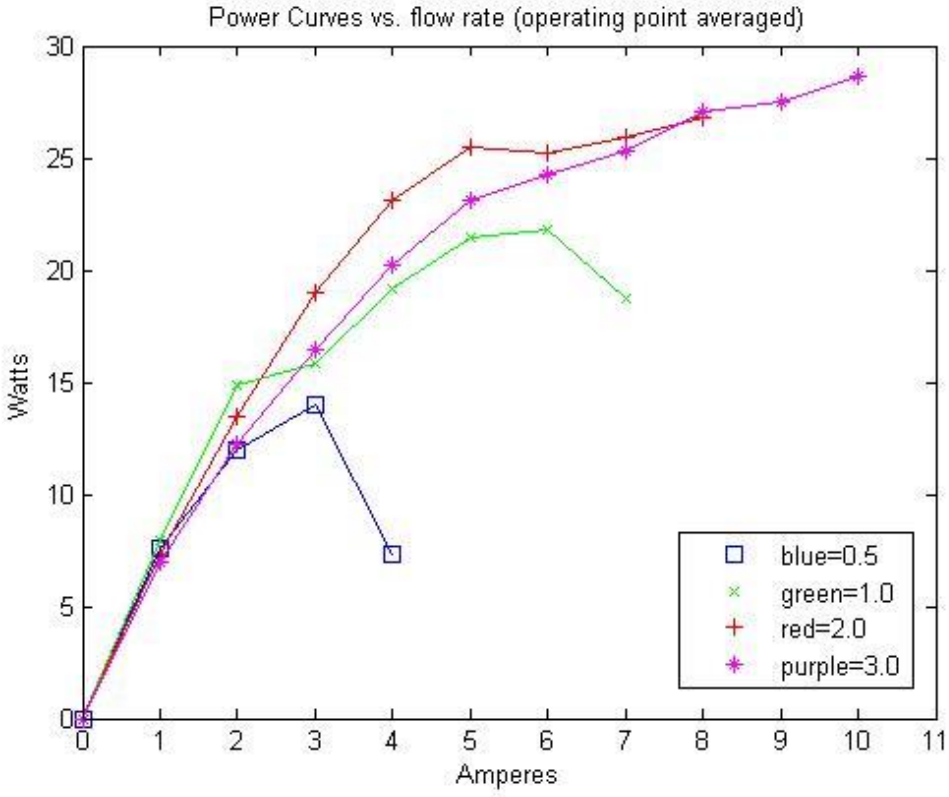

Figure 2.5. Power curves vs. flow rate.

2.3. DBFC Frequency Response and equivalent circuit

The method used for characterizing the DBFC is introduced in [22]. EIS or electrochemical impedance spectroscopy is simply frequency response analysis (FRA) applied to electrochemical systems.

With this technique, the frequency domain characteristics can be determined by injecting a known sinusoidal current with amplitude I_M and frequency ω as in (2.1). Furthermore, the output voltage of the circuit is recorded in the form of (2.2) which has a different amplitude V_M and phase shift θ but is at the same frequency. Using Euler's relationship in (2.3), (2.1) and (2.2) are shown again in their complex forms in (2.4) and (2.5). This allows for the computation of complex impedance Z versus complex frequency $j\omega$ as in (2.6) which has a fixed magnitude. Thus, sweeping the frequency of the injected signal (2.1) allows for the collection of a series of impedance points versus frequency and ultimately the construction of the Bode or Nyquist plots of the impedance of the device under test.

$$I(\omega) = I_M cos(\omega t) \tag{2.1}$$

$$V(\omega) = V_M \cos(\omega t - \theta) \tag{2.2}$$

$$e^{j\omega t} = cos\omega t + jsin\omega t \tag{2.3}$$

$$I(j\omega) = I_M e^{j\omega t} \tag{2.4}$$

$$V(j\omega) = V_M e^{j(\omega t - \phi)} \tag{2.5}$$

$$Z(j\omega) = \frac{V(j\omega)}{I(j\omega)} = \frac{V_M}{I_M} e^{j\phi} \tag{2.6}$$

The theory above was applied to the DBFC using a custom test setup depicted in Figure 2.6. This test setup consisted of the DBFC stack, EIS equipment, an adjustable electrical load, an electrochemical interface (Solartron SI 1287), and FRA software analysis tool known as "Z-plot". The perturbing AC signal was applied at various constant load conditions of 2, 3, and 4 amps with a frequency sweep range of 1Hz to 20KHz while the frequency response was recorded. The resulting bode plot as well as a nyquist plot of the same data are shown in Figures 2.7 and 2.8.

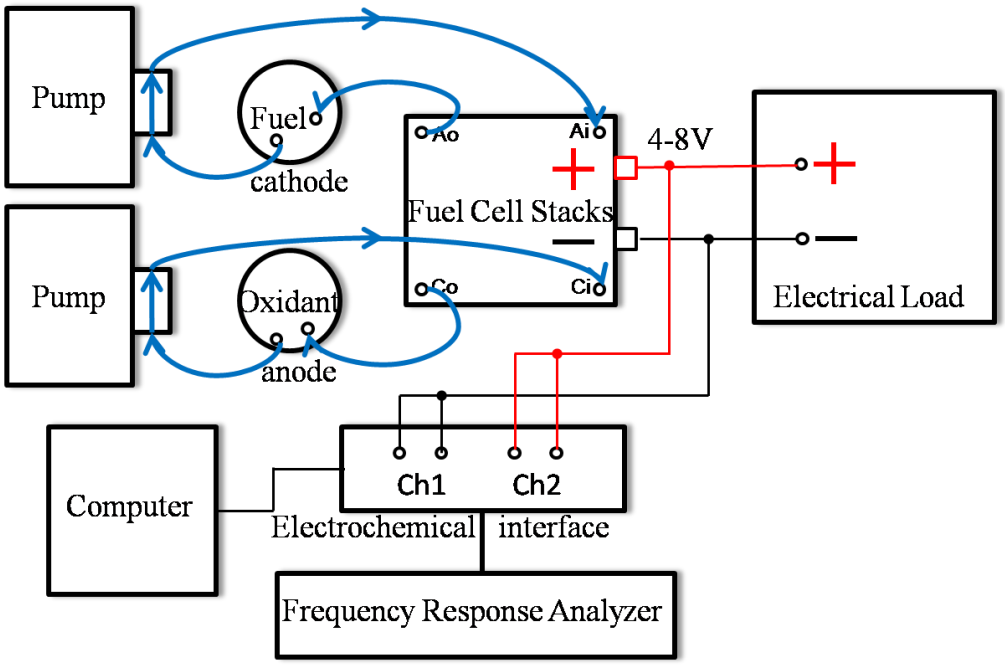

Figure 2.6. Electrochemical impedance spectroscopy test setup.

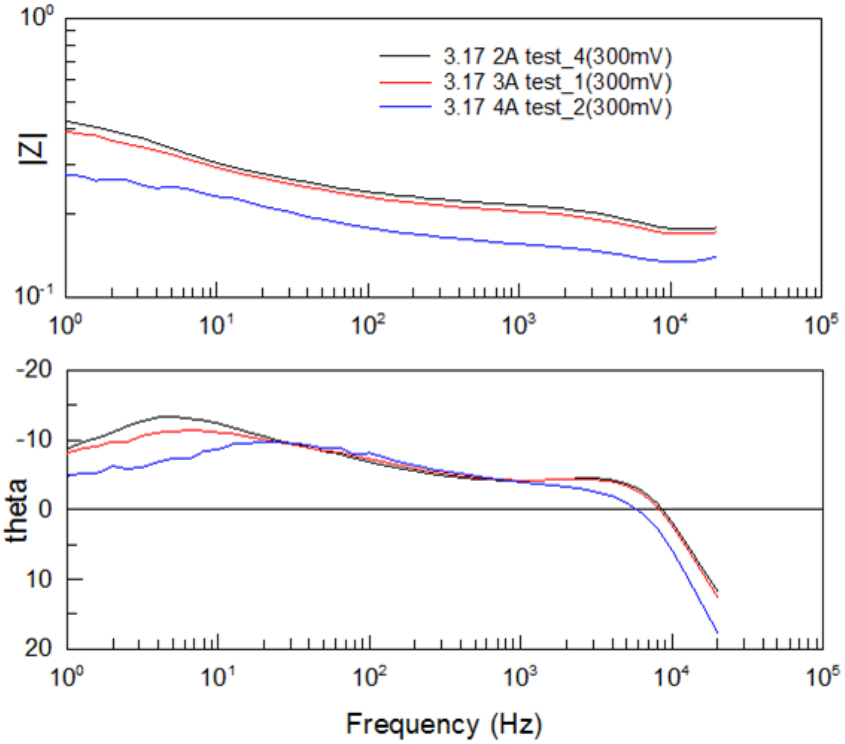

Figure 2.7. Bode plot of the results of the DBFC frequency response analysis. The 3 curves are representative of 3 independent tests that utilized 2, 3, and 4 amp constant current loads.

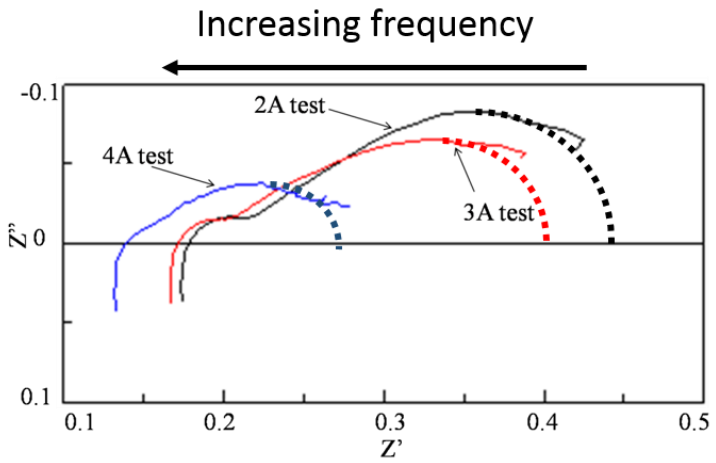

Figure 2.8. Nyquist representation of the frequency response analysis data.

The shape of the nyquist plot in Figure 2.8 allows for the direct derivation of an equivalent circuit. Firstly, the “semi-circles” (more obviously present in the 2 and 3 amp tests) had dashed lines added to pronounce their shape and low-frequency intercept

points. These “semi-circles” correlate to two parallel R-C circuits present in the DBFC equivalent circuit while the high frequency intercept represents a pure series resistance. The circuit described by this model can be seen in Figure 2.9.

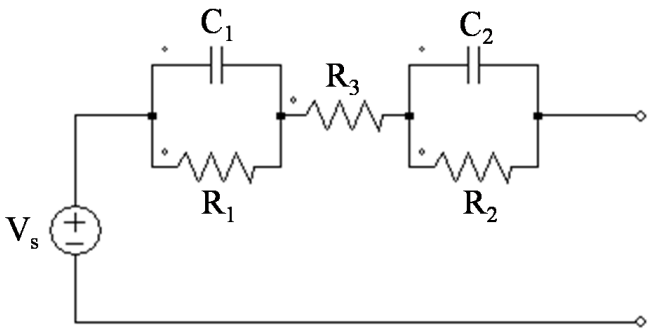

Figure 2.9. DBFC equivalent circuit.

Since the high frequency interrupt directly correlates to the series resistor R_3 its value can be directly observed. Each of the two semi-circle per constant current test has a parallel RC circuit time constant τ associated with it. Furthermore, ω_{max} is defined as the frequency for which the imaginary component of each semi-circle is most negative. These relationships are summarized in (2.4):

$$\tau = RC, \omega_{max} = 1/\tau \tag{2.4}$$

Using the above methods the parameters of the equivalent circuit can be derived. For example, consider the 3A test: The high frequency intercept is approximately at 0.17, hence $R_3 = 0.17$. Further, the low frequency intercept is approximately 0.4, and thus $R_1 + R_2 + R_3 = 0.4$ and $R_1 + R_2 \cong 0.23$. Using the software tool Z-plot, ω_{max} was found for each semi-circle to be $\omega_1 \cong 24.55$ and $\omega_2 \cong 1602.56$. The diameter of each semi-circle roughly correlates to the resistance of each parallel circuit, and hence $R_1 \cong 0.268$ and $R_2 = 0.052$. Using these values the capacitances can also be calculated. Using

this same procedure values for each of the constant current tests was derived and those values are in table 2.2.

It is possible to obtain a more accurate circuit description based on the test data, however it may not be tractable for control design purposes. Further, using some of the very detailed data that was acquired means that the test setup should be greatly scrutinized so as not to be modeling aspects that were not truly introduced by the characteristics of the DBFC.

The total series resistance as indicated by table 2.2 ranges from 0.284 Ohms to 0.489 Ohms. One of the major focus of this thesis is control design with the DBFC as a source, and later chapters will design a controller with DBFC impedances varying from 0.025, 0.25, and 2.5 Ohms. As will later be shown, it possible to provide a number of great benefits by including a supercapacitor at the input of the converter, including negating the capacitances of the fuel cell, improving the overall system transient response, and providing an energy storage mechanism for remote startup. For that reason, the DBFC can be simplified and considered a voltage source with series impedance for the purposes of control design.

Table 2.2. Equivalent circuit parameter values for various DBFC EIS tests.

Load Current	R_1	R_2	R_3	C_1	C_2
2A	0.121 Ω	0.151 Ω	0.179 Ω	0.008F	0.001F
3A	0.268 Ω	0.052 Ω	0.172 Ω	0.152F	0.012F
4A	0.082 Ω	0.081 Ω	0.138 Ω	0.188F	0.011F

Chapter 3: Converter Modeling

3.1. State space modeling

For time-invariant systems, the state space model of a system is typically presented in the form of (3.1). Here *x* is a Mx1 vector representing M state variables of the system being modeled, $\dot{x}$ is the derivative of that vector, *u* is an Nx1 vector for N inputs, *y* is an Px1 vector for P system outputs, and *A,B,C,D* are the time invariant matrices that describe the dynamics of the system.

$$\dot{x} = Ax + Bu \tag{3.1}$$

$$y = Cx + Eu$$

3.2 State space averaging technique

Power electronic converters typically involve non-linear dynamics introduced by MOSFET on/off switching and diodes which conduct current in one direction and block in another. However, it is possible to create a state space model for each switching interval of a converter, treating each case as its own linear circuit. Once that has been done an average model of the system can be created from a weighted average of each interval. That weighting is based on the time spent in each linear circuit position which is dictated by duty cycle. This approach results in the following 2 sets of state space system equations:

$$K\dot{x} = A_1 x + B_1 u \tag{3.2}$$

$$y = C_1 x + E_1 u$$

$$K\dot{x} = A_2 x + B_2 u \tag{3.3}$$

$$y = C_2 x + E_2 u$$

The addition of the MxM matrix of constant coefficients K will become apparent once this approach has been directly applied to power electronics switching converters. Based on (3.2) and (3.3), one can then take the duty-cycle weighted sum of these states to create an average model of the system:

$$A = d * A_1 + d' * A_2 \tag{3.4}$$

$$B = d * B_1 + d' * B_2$$

$$C = d * C_1 + d' * C_2$$

$$E = d * E_1 + d' * E_2$$

Where *d* is duty cycle and *d'* is the complement of *d* or *1-d.*

3.2.1 DC solution to state space model

The conventional approach to average state space modeling of switching converters is to select the capacitor voltages and inductor currents as the states of the system. This has several advantages. The first advantage is realized when noting that switching converters are operating in steady state then the principles of charge balance and inductor volt-second balancing apply. They dictate that for one switching period of a converter the inductor current and capacitor voltages within the circuit do not change. Hence, since these quantities were selected as the states of the system, their time

derivatives in steady state are equal to 0 and the DC equations of the system are as in (3.5):

$$0 = AX + BU \tag{3.5}$$

$$Y = CX + EU$$

In (3.5), the capitalized quantities $X, Y, and\ U$ represent the steady state values of $x, y, and\ u$. Using matrix algebra the solution to these DC equations can be found to be

$$X = -A^{-1}BU \tag{3.6}$$

$$Y = (-CA^{-1}B + E)U$$

3.2.2 Derivation of small signal model

It is desirable to obtain a frequency domain model of a converter for control modeling and estimating system dynamics. Based on the DC solutions presented in (3.6) which were derived in the previous section it is possible to create such a model. The DC solution is chosen as the “quiescent” operating point about which a dynamic small signal model can be derived by perturbing and then linearizing around this point. This concept is a standard approach to linearizing non-linear models. In essence it holds that when considering the dynamics of a system focused around a single area, the local dynamics are approximately linear. Hence, applying "small signal” disturbances (perturbations) around this quiescent operating point allows one to create an approximated linear model for the system.

To begin this procedure, the quiescent operating points $X, Y, U, and\ D$ are replaced by the steady state value plus a small signal perturbation:

$$< x(t) >_{Ts} = X + \hat{x}(t) \tag{3.7}$$

$$< u(t) >_{Ts} = U + \hat{u}(t)$$

$$< y(t) >_{Ts} = Y + \hat{y}(t)$$

$$d(t) = D + \hat{d}(t), d'(t) = D' + \hat{d}'(t)$$

Next, consider the inter-period dynamics of the model with these new average value points. In the first subinterval of the converter, the states of the system change as (3.8):

$$\frac{dx(t)}{dt} = k^{-1}(A_1 < x(t)_{Ts} > + B_1 < u(t)_{Ts} >) \tag{3.8}$$

Since the total converter period has length T_s, the first interval length is dictated by duty cycle and has length $d * T_s$. Therefore the value of the system states at the end of the first subinterval can be expressed as

$$final\ value = initial\ value + (interval\ length * slope) =$$

$$x(dT_S) = x(0) + (dT_s)k^{-1}(A_1 < x(t)_{Ts} > + B_1 < u(t)_{Ts} >). \tag{3.9}$$

Similar to (3.8), in the second subinterval the system states change as

$$\frac{dx(t)}{dt} = k^{-1}(A_2 < x(t)_{Ts} > + B_2 < u(t)_{Ts} >). \tag{3.10}$$

Therefore, the state vector at the end of the switching period can be expressed as

$$x(T_s) = x(dT_S) + (d'T_s)k^{-1}\left(A_2 < x(t)_{T_s} > + B_2 < u(t)_{T_s} >\right) = \tag{3.11}$$

$$x(0) + (dT_s)k^{-1}(A_1 < x(t)_{Ts} > + B_1 < u(t)_{Ts} >)$$

$$+ (d'T_s)k^{-1}\left(A_2 < x(t)_{T_s} > + B_2 < u(t)_{T_s} >\right).$$

Rearranging terms yields

$$x(T_s) = x(0) + T_s k^{-1}(dA_1 + d'A_2) < x(t) >_{Ts} + T_s k^{-1}(dB_1 + d'B_2) < u(t) >_{Ts} \tag{3.12}$$

In this average model, the derivative of $< x(t) >_{Ts}$ for one switching period can be approximated as

$$\frac{d<x(t)>_{Ts}}{dt} \cong \frac{x(T_S) - x(0)}{T_S}. \tag{3.13}$$

It can be seen that subtracting $x(0)$ from both sides of (3.11) and then dividing both sides by T_s puts the equation in the form of (3.13). From there, left-multiplying both sides of the equation by k yields

$$k\frac{d<x(t)>_{Ts}}{dt} = (dA_1 + d'A_2) < x(t) >_{Ts} + (dB_1 + d'B_2) < u(t) >_{Ts} \tag{3.14}$$

Next, the average terms can be replaced by their quiescent operating point plus disturbance terms.

$$k\frac{d\left(X + \hat{x}(t)\right)_{Ts}}{dt} =$$

$$\left(\left(D + \hat{d}(t)\right)A_1 + \left(1 - \left(D + \hat{d}(t)\right)\right)A_2\right)\left(X + \hat{x}(t)\right)_{Ts} +$$

$$\left(\left(D+\hat{d}(t)\right)B_1+\left(1-\left(D+\hat{d}(t)\right)\right)B_2\right)\left(U+\hat{u}(t)\right)_{Ts} \tag{3.15}$$

Considering (3.4), (3.15) can be simplified to

$$k\frac{d\left(X+\hat{x}(t)\right)_{Ts}}{dt}=$$

$$\left(A+\hat{d}(t)A_1+\hat{d}(t)A_2\right)\left(X+\hat{x}(t)\right)_{Ts}+$$

$$\left(B+\hat{d}(t)B_1+\hat{d}(t)B_2\right)\left(U+\hat{u}(t)\right)_{Ts} \tag{3.16}$$

Multiplying through while cancelling second order terms and factoring the results in

$$K\frac{d\hat{x}(t)}{dt}=AX+BU+A\hat{x}(t)+B\hat{u}(t)+\hat{d}(t)[(A_1-A_2)X+(B_1-B_2)U] \tag{3.17}$$

Because of (3.6) the DC terms are by definition equal to 0. Therefore, the final result is shown in (3.18):

$$K\frac{d\hat{x}(t)}{dt}=A\hat{x}(t)+B\hat{u}(t)+\{(A_1-A_2)X+(B_1-B_2)U\}\hat{d}(t) \tag{3.18}$$

$$\hat{y}=C\hat{x}(t)+E\hat{u}(t)+\{(C_1-C_2)X+(E_1-E_2)U\}\hat{d}(t)$$

The substitutions in (3.19) make the transfer function derivations more straightforward:

$$\alpha=K^{-1}A \tag{3.19}$$

$$\beta=K^{-1}B$$

$$\gamma=K^{-1}\{(A_1-A_2)X+(B_1-B_2)U\}$$

$$\zeta = (C_1 - C_2)X + (E_1 - E_2)U$$

With these equations, the overall input-to-output transfer function and control-to-output transfer functions can be calculated via (3.20) and (3.21), respectively:

$$G_{vg}(s) = C(sI - \alpha)^{-1}\beta + E \tag{3.20}$$

$$G_{vd}(s) = C(sI - \alpha)^{-1}\gamma + \zeta \tag{3.21}$$

To summarize the above derivations, the state space modeling equations allows the designer to find the average state space model based on (3.1)-(3.4), then find the steady state solution to the states and inputs of the system using (3.6), and finally determine the line-to-output and control-to-output transfer functions as outlined in (3.20) and (3.21). The transfer functions mentioned for an ideal boost converter in terms of component values and average duty cycle values (with the output variable specifically being output voltage) are commonly available and well known to be (3.22) and (3.23):

$$G_{vd}(s) = \frac{V_o}{D'} \frac{1 - \frac{sL_1}{D'^2 R_o}}{1 + \frac{sL_1}{D'^2 R_o} + \frac{s^2 L_1 C_o}{D'^2}} \tag{3.22}$$

$$G_{vg}(s) = \frac{1}{D'} \frac{1}{1 + \frac{sL_1}{D'^2 R_o} + \frac{s^2 L_1 C_o}{D'^2}} \tag{3.23}$$

3.2.3 Derivation of small signal model for 3-period system

This section is an extension of the previous section. In the case of a dual-interleaved converter as in Figure App.1 in appendix I, there are 3 circuit configurations that occur during one period of converter switching assuming the duty cycle is not equal to exactly 50%. If the same principles of weighted averaging based on duty cycle values

are applied, the result is that nearly the exact same steady state solutions and converter transfer functions can be derived as was done for a single-phase converter. Depending on whether the duty cycle is less than or greater than 50% the 3 periods of this converter will be different. When duty cycle is less than 50%, the 3 periods are: leg (1) has lower switch on and leg (2) has upper switch on, both legs have upper switches on, then leg (1) has upper switch on and leg (2) has lower switch on. When duty cycle is greater than 50%, the 3 periods are: leg (1) lower switch on and leg (2) upper switch on, both legs have lower switches on, then leg (1) has upper switch on and leg (2) has lower switch on. The derivation in appendix one is for the case where duty cycle is less than 50% but the theory is extensible to both cases.

3.3 State space model of boost converters

In this section the theories of sections 3.1 and 3.2 will be applied to actual power converter topologies, specifically a non-isolated DC-DC boost converter. Two major simplifying assumptions are made in the most basic model that will be presented first. The first is that a MOSFET is an ideal short (zero resistance, inductance, or capacitance) from drain-to-source when it is biased “on” via a positive gate-source voltage and that it acts as an ideal diode (due to its body diode) when it is “off” and there is no gate-source voltage bias. The second is that both the stand-alone diode and the MOSFET body diode are also ideal shorts when positive current is flowing into their cathodes and an open circuit (infinite resistance) when reverse biased, i.e. when there is a positive anode-cathode voltage across the diode no current will flow.

With these simplifications one could easily determine both of the equations of an ideal buck, boost, or buck-boost converter when the switching device is in the “on” position and when the switching device is in the “off” position. In the following sections, increasingly specific models will be derived that incorporate more and more non-idealities such as the DBFC impedance, MOSFET on-state resistances and capacitor equivalent series resistances. While the following sections only derive the models of non-isolated boost converters, this approach is extensible to all switching converters that utilize inductors, capacitors, and semiconductor switching/diodes to achieve power conversion.

3.3.1. Simplified model

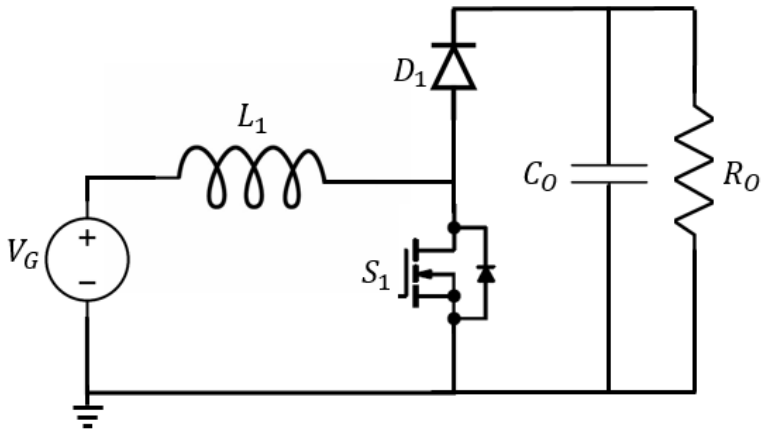

Figure 3.1. Ideal boost converter circuit with purely resistive load.

For an ideal boost converter circuit such as Figure 3.1, one can use the procedure outlined in the state-space modeling sections to determine the theoretical line-to-output and control-to-output transfer functions. To do these, equations that describe the system dynamics are required for both switching intervals. As is the standard procedure, all

inductor currents and capacitor voltages are chosen as the state variables of the system. The inputs and outputs are more flexible and can for example be input/output voltages or currents. In this case, the input voltage source is chosen as the input and the input current I_G is chosen as the output since the output voltage information will already be contained in the capacitor voltage. This also means that the control-to-output transfer function will provide dynamic information about the input current changing with respect to duty cycle changes. These selections result in state space model variables seen in (3.24)-(3.26):

$$x = \begin{bmatrix} V_{Co} \\ i_{L1} \end{bmatrix} \tag{3.24}$$

$$y = [I_G] \tag{3.25}$$

$$u = V_g \tag{3.26}$$

Referring to the circuit of Figure 3.1 the "on" state of switch S1 is first considered where switch S1 is considered a perfect short while D1 is considered a perfectly blocking diode (open circuit) as there will be some positive output voltage.

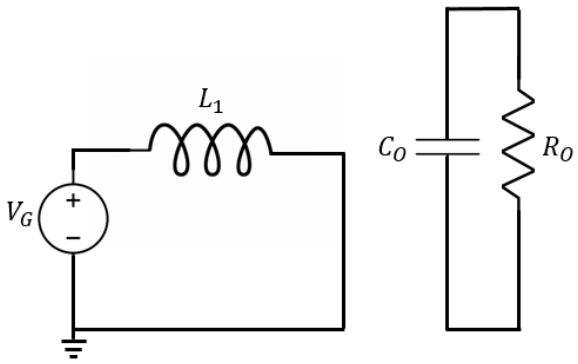

Figure 3.2. The circuit of Figure 3.1 when switch S1 is on the "on" state and diode D1 is a perfect open circuit.

(3.27)-(3.29) are derived to describe the derivative of the state variables and output variable in terms of the state variables and input. (3.30) and (3.31) then summarize these equations in matrix form.

$$C_o \frac{dV_{Co}}{dt} = -\frac{V_o}{R_o} = -\frac{V_{Co}}{R_o} \tag{3.27}$$

$$L_1 \frac{di_{L1}}{dt} = V_G \tag{3.28}$$

$$I_G = i_{L1} \tag{3.29}$$

$$\begin{bmatrix} C_o & 0 \\ 0 & L_1 \end{bmatrix} \begin{bmatrix} \frac{dV_{Co}}{dt} \\ \frac{di_{L1}}{dt} \end{bmatrix} = \begin{bmatrix} -\frac{1}{R_o} & 0 \\ 0 & 0 \end{bmatrix} \begin{bmatrix} V_{Co} \\ i_{L1} \end{bmatrix} + \begin{bmatrix} 0 \\ 1 \end{bmatrix} V_G \tag{3.30}$$

$$I_G = [0 \quad 1] \begin{bmatrix} V_{Co} \\ i_{L1} \end{bmatrix} + [0] V_G \tag{3.31}$$

In the second half of the switching cycle switch S1 is off and thus considered an open circuit while diode D1 is conducting current from in the input voltage source and input inductor to the load as can be seen in Figure 3.3. In this case the equations for the circuit are described in (3.32)-(3.34) and are in matrix form in (3.35) and (3.36).

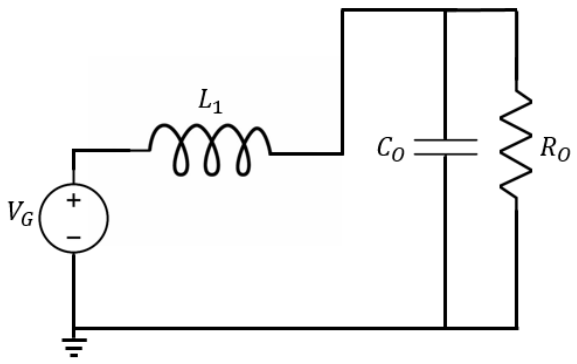

Figure 3.3. The circuit of Figure 3.1 when switch S1 is on the “off” state and diode D1 is conducting as a perfect short.

$$C_o \frac{dV_{Co}}{dt} = i_{L1} - i_o = i_{L1} - \frac{V_o}{R_o} = i_{L1} - \frac{V_{Co}}{R_o} \tag{3.32}$$

$$L_1 \frac{di_{L1}}{dt} = V_G - V_o = V_G - V_{Co} \tag{3.33}$$

$$I_G = i_{L1} \tag{3.34}$$

$$\begin{bmatrix} C_o & 0 \\ 0 & L_1 \end{bmatrix} \begin{bmatrix} \frac{dV_{Co}}{dt} \\ \frac{di_{L1}}{dt} \end{bmatrix} = \begin{bmatrix} -\frac{1}{R_o} & 1 \\ -1 & 0 \end{bmatrix} \begin{bmatrix} V_{Co} \\ i_{L1} \end{bmatrix} + \begin{bmatrix} 0 \\ 1 \end{bmatrix} V_G \tag{3.35}$$

$$I_G = \begin{bmatrix} 0 & 1 \end{bmatrix} \begin{bmatrix} V_{Co} \\ i_{L1} \end{bmatrix} + [0] V_G \tag{3.36}$$

From the equations that describe each portion of one switching interval the average state space matrices can be calculated from (3.4) for a given duty cycle. Subsequently, the steady state solution to the states of the system using (3.6) and finally the line-to-output and control-to-output transfer functions as outlined in (3.20) and (3.21) can be derived. Note that if this procedure was followed then the result would differ from the transfer functions described in (3.22) and (3.23) because here the output was chosen the be the current I_g of the ideal source V_G. However, if the output been selected as the output voltage the transfer functions would match identically.

3.3.2. With DBFC impedance

This section extends the results of the previous section while also including the DBFC impedance. Both of the sub circuits within one switching interval are shown in Figure 3.4. The same state variables, input variable (input voltage), and output variable

(input current) are used. In this case, the equations that describe capacitor current and input current I_G are exactly the same as in the previous sections for both switching intervals. However, the inductor voltage $L_1 \frac{dI_{L1}}{dt}$ takes a slightly modified form as in (3.37) and (3.38) for switching intervals 1 and 2, respectively.

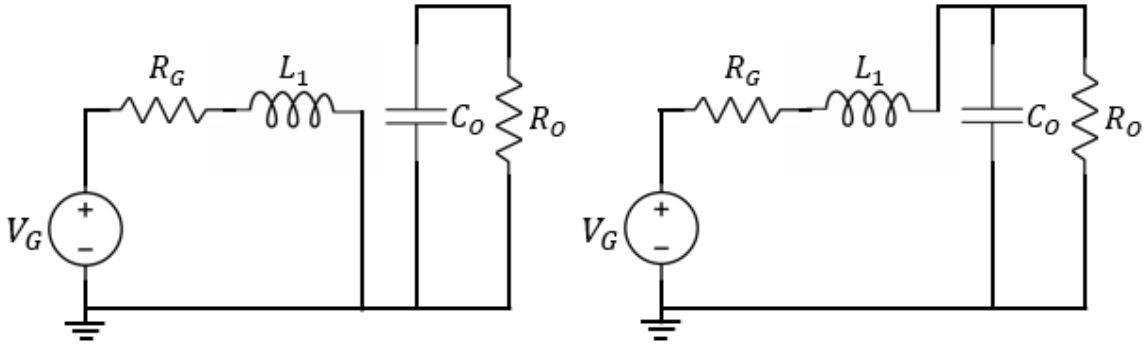

Figure 3.4. Sub-circuits for the boost converter model that also includes a resistive source impedance modeling that of the DBFC's.

$$V_{L1} = L_1 \frac{di_{L1}}{dt} = V_G - i_{L1} R_g \tag{3.37}$$

$$L_1 \frac{di_{L1}}{dt} = V_G - i_{L1} R_g - V_o = V_G - i_{L1} R_g - V_{Co} \tag{3.38}$$

With these equations, the averages state space matrices can be computed from 3.4 and are found to be as shown in (3.39)-(3.42) where *D* is the duty ratio and *D' = 1 - D*.

$$A = DA_1 + D'A_2 = \begin{bmatrix} -\frac{1}{R_o} & D' \\ -D' & -R_g \end{bmatrix} \tag{3.39}$$

$$B = DB_1 + D'B_2 = \begin{bmatrix} 0 \\ 1 \end{bmatrix} \tag{3.40}$$

$$C = DC_1 + D'C_2 = [0 \quad 1] \tag{3.41}$$

$$E = DE_1 + D'E_2 = 0 \tag{3.42}$$

With these results, the DC solutions to the circuit can be found via (3.6) and furthermore the control-to-input-current transfer function from (3.21). This will differ from the transfer function $G_{vd}(s)$ previously mentioned because that was the standard form for the control-to-output-voltage transfer function where in this case the output variable is source current. The result of this new transfer function is shown in (3.43).

$$G_{id}(s) \triangleq \frac{\tilde{\imath}_L}{\tilde{d}} = \frac{R_o C_o V_o s + V_o + (1-D) R_o I_L}{R_o C_o L s^2 + \left(L + R_g R_o C_o\right) s + R_{fc} + (1-D)^2 R_o} \tag{3.43}$$

3.3.3. Addition of supercapacitor

Previously the impact of the DBFC impedance has been factored into converter transfer functions. Now, the transfer functions for a topology that includes supercapacitors at the converter input will be derived. Two new components are introduced into the circuit: the supercapacitor itself C_s and it's equivalent series resistance (ESR) R_{Cs}. Since another capacitor has been introduced into the circuit, the additional state V_{Cs} has also been introduced. Thus the matrices A, B, C, and E are now 3x3, 3x1, 1x3, and 1x1 respectively. The diagonal matrix of constant coefficients now appears as in (3.44).

$$K = \begin{bmatrix} C_o & 0 & 0 \\ 0 & L1 & 0 \\ 0 & 0 & C_s \end{bmatrix} \tag{3.44}$$

In this case, the output variable of interest will be output voltage so that the control-to-output-voltage transfer function can be directly derived.

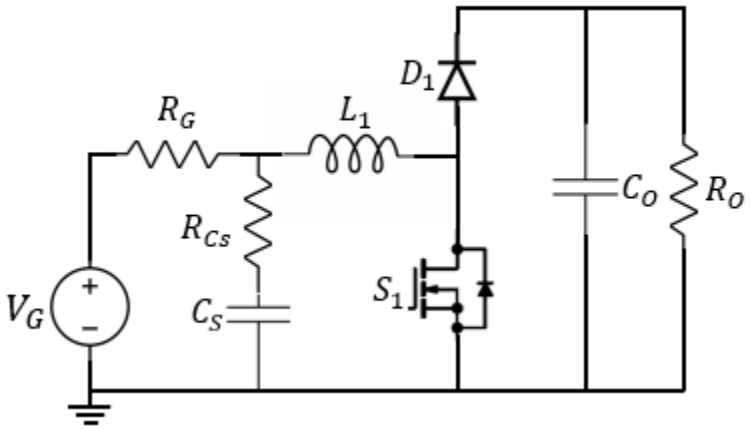

Figure 3.5. Boost converter circuit that now includes the DBFC source impedance Rfc but also an input supercapacitor Cs as well as its ESR Rcs.

After deriving the equations for each switching interval of the converter shown in Figure 3.5 the matrices for each switching interval are shown in (3.45)-(3.49). These equations allow for the computation of the control-to-output transfer function via (3.6) and subsequently (3.20) and (3.21).

$$A_1 = \begin{bmatrix} -\frac{1}{R_o} & 0 & 0 \\ 0 & -\frac{R_{Cs}R_{fc}}{R_{fc}+R_{Cs}} & \frac{R_{fc}}{R_{fc}+R_{Cs}} \\ 0 & -\frac{R_{fc}}{R_{fc}+R_{Cs}} & \frac{R_{fc}}{R_{Cs}(R_{fc}+R_{Cs})} - \frac{1}{R_{Cs}} \end{bmatrix} \tag{3.45}$$

$$B_1 = B_2 = \begin{bmatrix} 0 \\ \frac{R_{Cs}}{R_{Cs}+R_{fc}} \\ \frac{1}{R_{fc}+R_{Cs}} \end{bmatrix} \tag{3.46}$$

$$C_1 = C_2 = [1 \quad 0 \quad 0] \tag{3.47}$$

$$E_1 = E_2 = 0 \tag{3.48}$$

$$A_2 = \begin{bmatrix} -\frac{1}{R_o} & 1 & 0 \\ -1 & -\frac{R_{Cs}R_{fc}}{R_{fc}+R_{Cs}} & \frac{R_{fc}}{R_{fc}+R_{Cs}} \\ 0 & -\frac{R_{fc}}{R_{fc}+R_{Cs}} & \frac{R_{fc}}{R_{Cs}(R_{fc}+R_{Cs})} - \frac{1}{R_{Cs}} \end{bmatrix} \tag{3.49}$$

3.3.4. Output cap ESR and Interleaved models

Compared to a buck converter, the plant model of a standard boost converter introduces a right-half-plane zero in the plant transfer function that makes achieving high-bandwidth closed loop voltage control more difficult. Furthermore, modeling the output capacitor equivalent series resistance (ESR) introduces yet another zero in plant transfer function. Typically, with proper component selection and board layout this ESR can be minimized and the effects of the zero occur at frequencies beyond the concern of closed loop control, specifically at $1/(2\pi C_o R_{Co})$. Additionally, some designs employ interleaved phases to achieve effects like reduced input current ripple and lower peak current stresses on the components of each phase. It turns out that neither the output capacitor ESR nor the interleaved boost converter have a significant impact on the control design problem at hand. However, their plant models were derived and can be seen in Appendix II.

Chapter 4: System control design

4.1. Examining effect of DBFC non-ideal impedance

Previously the control-to-output-voltage transfer function $G_{vd}(s)$ was derived for boost converter topologies with varying degrees of circuit detail as well as with and without supercapacitors. To understand the effect of the DBFC impedance, first consider the standard control-to-output transfer function $G_{vd}(s)$ with no DBFC impedance, before the addition of supercapacitors, and neglecting output capacitor ESR (which has negligible impact on overall transfer function assuming ESR is kept small). This transfer function in its zero/pole/gain form can be seen in (4.1). In (4.1) there is a constant gain k, a right-half-plane zero, and there are two poles which may be a complex-conjugate pair or separate real-valued poles. The right-half-plane zero is a well-known and problematic component of boost converter control-to-output transfer function because it introduces a -90 degree phase shift in the frequency domain around frequency α which leads to bandwidth reduction. Note that the neglected output capacitor ESR also does this, but if ESR is small then it tends to be a high frequencies beyond the concern of conventional control design. Further, when the DBFC impedance is zero or small valued, the poles in 4.1 are a complex conjugate pair that create a resonant peak in the gain plot and an additional -180 degree phase shift in phase. A good approximation of this transfer function can be seen in Figure 4.1 where the DBFC impedance is shown in various levels and $R_{fc} = 0.025\Omega$ approximating no impedance.

$$G_{vd}(s) = k\frac{s+\alpha}{(s-\beta)(s-\gamma)} \tag{4.1}$$

As the impedance of the DBFC increases and approaches its realistic value, several changes occur. Most notably the previously complex-conjugate pair poles tend towards becoming purely real valued. At this inflection point, further increasing of the DBFC impedance continues to reduce the frequency of one of the poles. This has two implications: the gain begins to "roll off" at 20dB/decade at lower frequencies reducing the bandwidth and the DC gain of the system is reduced.

The transfer function derived in section 3.3.2 included a source impedance for the DBFC. Using the values of table 4.1 a Bode plot was generated demonstrating how this transfer function varies as a function of DBFC impedance and can be seen in Figure 4.1.

Table 4.1. Values for control-to-output-voltage transfer function.

Parameter	Value
L	15uH
C_o	100uF
V_g	6 volts
$D\ (duty)$	0.5
R_o	24 Ohms
R_{fc}	Variable: [0.025, 0.25, 2.25] Ohms

4.2. Effect on conventional voltage control

Figure 4.2 shows a control block diagram for conventional feedback control of the boost converter output voltage. In includes a reference voltage v_o^*, a generic compensator $H(s)$ for which the details have not yet been explained, a block containing the plant control-to-output transfer function, and the actual output voltage v_o. For simplicity sake, this model neglects and constant gains introduced by the sensor feedback and pulse width modulation stage. When the final design is implemented, their gains can simply be compensated for by adjusting the overall gain of $H(s)$.

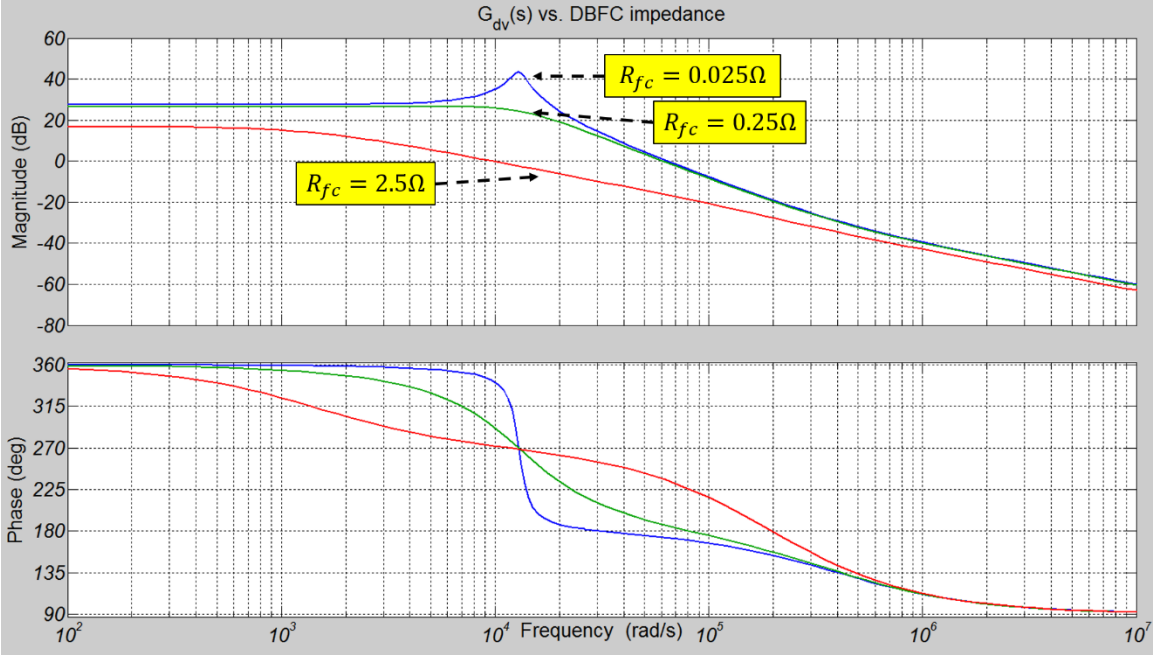

Figure 4.1. Bode plot of boost converter plant transfer function including the source impedance of the DBFC first derived in section 3.3.2.

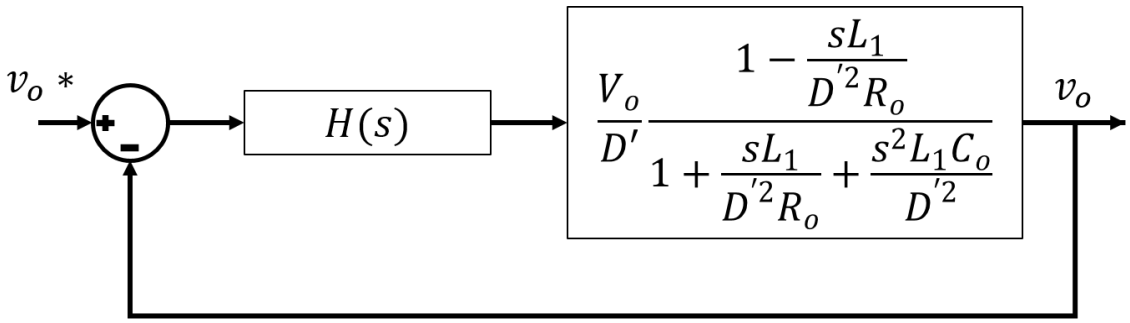

Figure 4.2. The structure of the voltage mode control scheme used. A reference v_o^* is supplied and the error term is the input to the compensator to be designed H(s). H(s) provides a duty cycle input to the control-to-output transfer function previously derived.

There are many options when choosing the compensator structure for boost converter control. Since this system will ultimately be controlled by a DSP, higher order compensators are acceptable as they needn't be implemented with physical components. The main constraints of the design are to achieve a stable feedback loop with $60°$ phase margin, at least 10dB of gain margin, zero steady state error, and ultimately to maximize the bandwidth of the controller under these conditions for optimal response time.

The control constraints result in a controller that is not of a standard proportional-integral (PI) controller, proportional-integral-derivative (PID) controller, type II or type III controller but rather a hybrid of these controllers. The form of this compensator is akin to a PID compensator with an additional real pole. Its form can be seen in (4.2) where $p > 0$.

$$H(s) = k\frac{1}{s}\frac{(s+z_1)^2}{(s+p)} \cong \left(k_p + \frac{k_i}{s} + k_d s\right)\frac{1}{s+p} \tag{4.2}$$

To achieve zero steady state error, a pole at the origin (integrator) is introduced. As was previously described, the control-to-output transfer function includes a double pole around the resonant frequency of the converter ω_{res} as described in (4.3). To mitigate the -40dB/decade gain reduction and -180 phase shift introduced by these poles, a double-real-zero pair is introduced into the compensator. Finally, to introduce a -20dB/decade at higher frequencies in the system, a real pole is added around 50 to 100 times the frequency of the zero pair.

$$\omega_{res} \cong \frac{1}{\sqrt{2\pi LC_o}} \tag{4.3}$$

Compensators for near zero DBFC impedance and with expected DBFC impedance were designed. The resulting bode plots of the loop gain can be seen in Figure 4.3. From this diagram it is clear that to obtain $60°$ phase margin, having significant DBFC impedance is disadvantageous. The system with little impedance achieved a crossover frequency of 419Krad/s while the system with impedance had less than half of that bandwidth at 184Krad/sec. Further, over the entire range of the bode plot the phase of

the system with higher DBFC impedance is closer to the 180° crossover implying the system may have more of an oscillatory response than desired by the $60°$ phase margin design constraint aimed for.

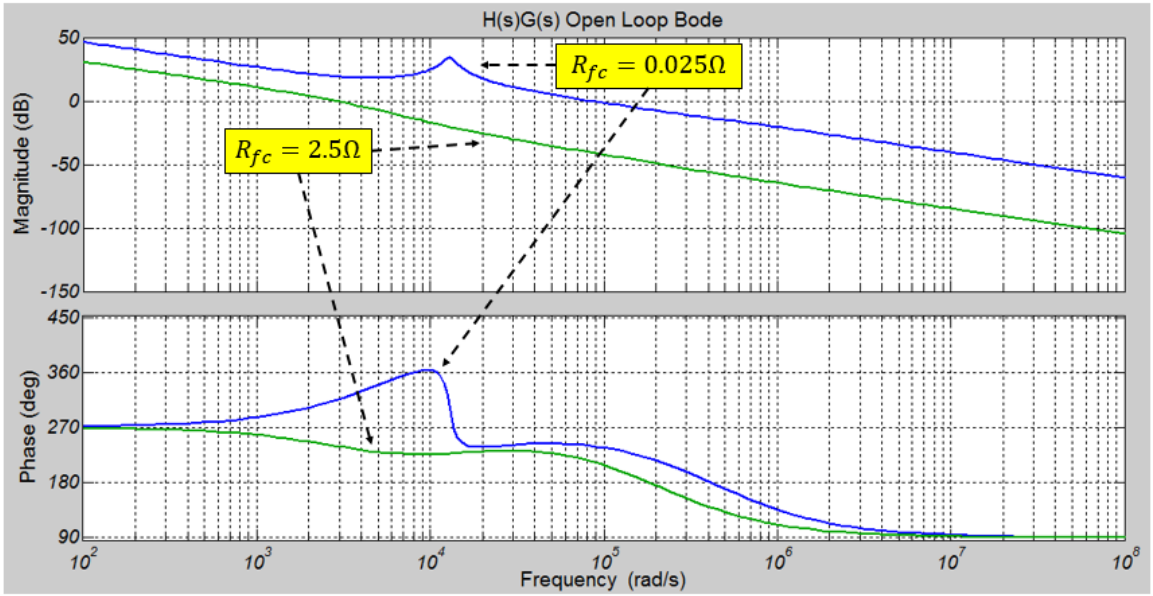

Figure 4.3. Loop gain H(s)G(s) optimized for two different fuel cell impedances.

4.3. Response Improvement with addition of Supercapacitor

First, the effect of adding a supercapacitor to the plant model of a boost converter that includes significant DBFC impedance ($R_{fc} = 2.5\Omega$) is examined. The transfer function for this topology was first derived in section 3.3. A bode plot of this plant for variable supercapacitor values and a fixed supercapacitor ESR of $10m\Omega$ is shown in Figure 4.4. As can be seen, even introducing a relatively small value of input capacitance of 250uF is enough to re-introduce the resonance seen in the standard plant transfer function with no DBFC impedance. However, there is still an approximate 10dB reduction in gain compared to the impedance-less transfer function over the approximate radian

frequency range [1~10K]. If the supercapacitor value is increased by a factor of 100 to $25mF$, the transfer fcuntion begins to closely resemble the original control-to-output transfer function for a boost converter with no input impedance. For control purposes, a value in this range may be acceptable, however as will be seen in chapter 5 the value of the supercapacitor is required to be larger anyways to power circuit peripherals during startup. Therefore, considering a supercapacitor value of $2.5F$, the plot again looks like the original transfer function even further extending into the low frequency range. This relationship can be summarized as in (4.4):

$$G_{dv_{cap}}(s)|_{C_s=2.5F} \cong G_{dv}(s)|_{R_{fc}=0} \tag{4.4}$$

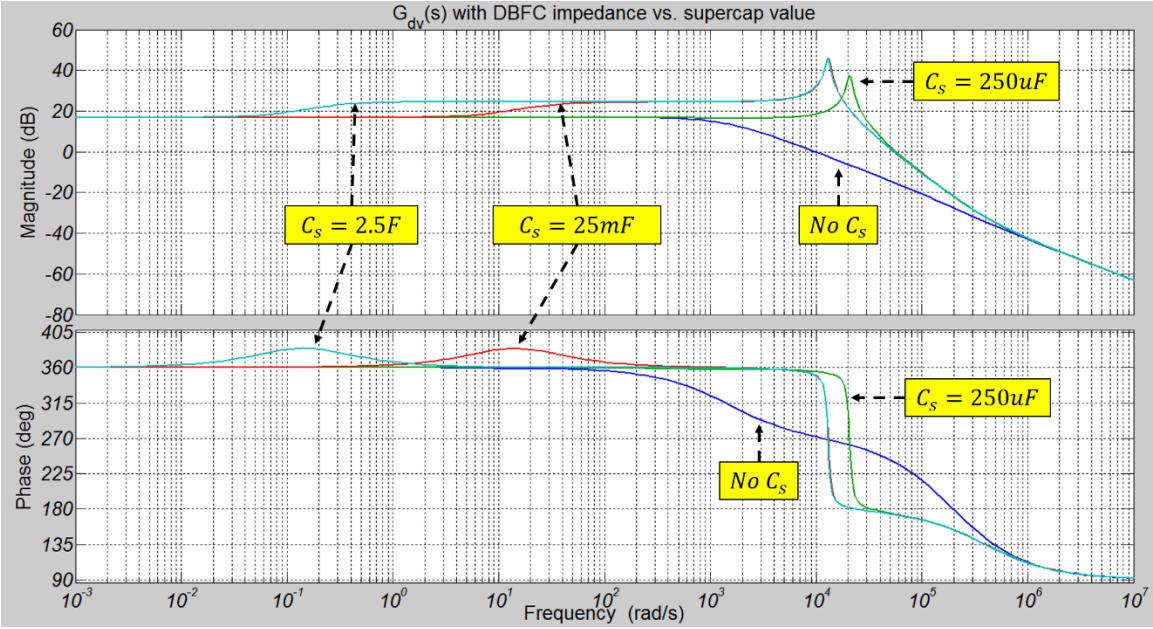

Figure 4.4. Boost converter plant transfer function with fixed DBFC source impedance and varying input supercapacitor sizes.

Next, control design for the cases where there is no supercapacitor input and where there is a 2.5F supercapacitor present will be considered. The compensator described in section 4.3 and its design steps were followed to derive the bode plot seen

in Figure 4.5. This figure makes the advantage of adding supercapacitors clear because for the same $60°$ achieved phase margin, the capacitor-less system has a crossover frequency of 3krad/sec while the system with the $2.5F$ capacitor has a crossover frequency of ~150krad/sec, a vast improvement.

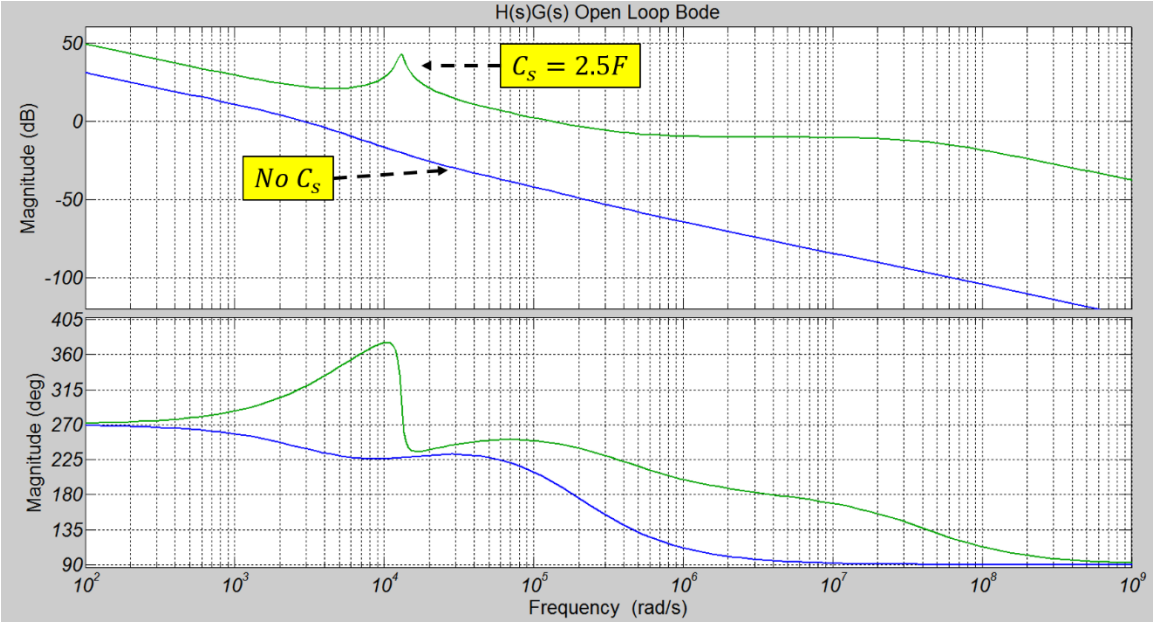

Figure 4.5. Loop gain H(s)G(s) function with fixed DBFC source impedance and varying input supercapacitor sizes. The system with the large input capacitance can be seen to have a much higher bandwidth and achieve higher phase margins in all lower frequency regions.

4.4. Supercapacitor Component Selection

Section 4.1 through 4.3 introduced theory on supercapacitor value selection in order to mitigate the effects of the DBFC impedance and achieve improved system frequency response. In this particular system design there is another constraint on supercapacitor size selection as a result of the system topology. The system needs to consider how much energy is required to be stored to initially power the fuel cell pumps, electronics, and any other balance of plant components for enough time until the fuel cell itself is producing enough energy to sustain this minimum 'startup' load. This minimum

supercapacitor value in terms of energy can be derived. The energy of a capacitor in general is given as in (4.5):

$$E_c = \frac{1}{2} C_s V^2 \tag{4.5}$$

In (4.5) C_s is the capacitance value of the supercapacitor in Farads and V is the voltage across the supercapacitor. This energy needs to be greater than the amount of power the pumps and control electronics consume for the entire amount of time it takes before the fuel cell is autonomously producing power as in (4.6).

$$\frac{1}{2} C_s V^2 \geq t_\Delta (P_{elec} + P_{pump}) \tag{4.6}$$

Here, t_Δ is the time from pump startup to when the fuel cell is producing enough power to run pumps and electronics autonomously, and P_{elec} and P_{pump} are the power consumed by the control circuitry and pumps. Lastly, there are two significant inefficiencies in the system to consider, η_1 and η_2. Firstly, when the system is starting up the supercapacitor voltage will be boosted to a regulated 12V output and that output will power the pumps and other DC-DC regulators powering the control circuitry. Hence, η_1 represents the efficiency of the boost converter itself to take into account energy lost in the boosting process. Secondly, while supercapacitor technology continues to improve, in practical situations a supercapacitor that has been charged to its rated voltage will experience some voltage decay due to internal losses. The experimental section will demonstrate how this discharging effect roughly follows an exponentially decaying curve that approaches some steady-state charge percentage in the range of 80%-90%. As a worst case approximation, this “final” value represents the second inefficiency η_2.

Finally, solving for the value of the supercapacitor gives

$$C_S \geq \frac{2t_\Delta(P_{elec}+P_{pump})}{(V^2)\eta_1\eta_2} \tag{4.7}$$

The time to reach autonomous operation, the power consumption of the pumps, the power consumption of the power electronics, the initial voltage on the supercapacitor and the converter efficiency are all system dependent parameters that either are chosen by design or experimentally obtained. In this particular design, 4 Taio Yuden 3 volt, 9 Farad supercapcitors were placed in series at the input of the converter to achieve an equivalent 12 volt, 2.25 Farad capacitance. This value is also large enough by a substantial margin to support the control design improvements mentioned in chapter 4.

Chapter 5: Simulation and Experimental Results

5.1. Control design with Matlab

Chapter 4 explained how proper value selection of the supercapacitor at the input of the boost converter can nullify the DBFC source impedance effects. Here the actual system values will be used to determine the true plant model and compensator values. The key component values are listed in table 5.1. Using these values, the control-to-output transfer function that includes both the DBFC impedance and input supercapacitors will be calculated based on the derivation of section 3.3.3. The result is shown in (5.1). Furthermore, a bode plot of this transfer function using the values of table 5.1 was previously shown in Figure 4.4.

Table 5.1. Component values of boost converter plant.

Parameter	Value
L	15uH
C_o	100uF
V_g	6 volts
$D\ (duty)$	0.5
R_o	24 Ohms
R_{fc}	2.25 Ohms
C_s	2.5 Farads
R_{C_s}	10 milliOhms

$$G_{vd}(s) = -7058.8\frac{(s-3.993e05)(s+0.09312)}{(s+0.2254)(s^2+1081s+1.67e08)} \tag{5.1}$$

Next, Matlab's™ Sisotool™ was used to graphically develop the controllers transfer function based upon the theory first presented in section 4.3. The structure of the control loop can be seen in Figure 4.2.

To implement the controller, first an integrator (pole at the origin) was included to remove steady state error. Next, the resonant peak of the plant was found to be approximately $10.3krad/sec$ via (5.2). In order to compensate for the steep $180°$ phase reduction due to the double resonant poles at this location, two real zeros were added slightly before this frequency at -5.83e+03 and -6.75e+03. Lastly, to reduce the gain at higher frequencies for noise reduction and to induce a smooth $-180°$ phase transition a real pole was added at a frequency above resonance at -4.23e+07. A screenshot of the final compensator design and its analytical expression can be seen in Figure 5.1. The loop gain bode plot of the compensator/plant $H(s)G(s)$ was already presented in Figure 4.5 in section 4.3 where the supercapacitor value was 2.5 Farads. This compensator yielded a gain margin of 10.3dB at 4.05e+06 radians/sec and a phase margin of $66.8°$ at 1.3e+05 radians/sec.

$$\omega_{res} = \frac{1}{\sqrt{2\pi LC_o}} \cong 10.3krad/sec \tag{5.2}$$

5.2. Simulink model validation

To validate the controller presented in the previous section a model was developed in Simulink™. The block diagram includes the exact plant model and controller coefficients presented in the previous sections. To test the system, an input reference step of 12 volts is generated a time $t = 0$. Furthermore, a "disturbance" is added to the reference to analyze reference tracking aside from the initial transient. This disturbance introduces ± 2 volt steps every millisecond. This Simulink block diagram can be seen in Figure 5.2 and the results in Figure 5.3.

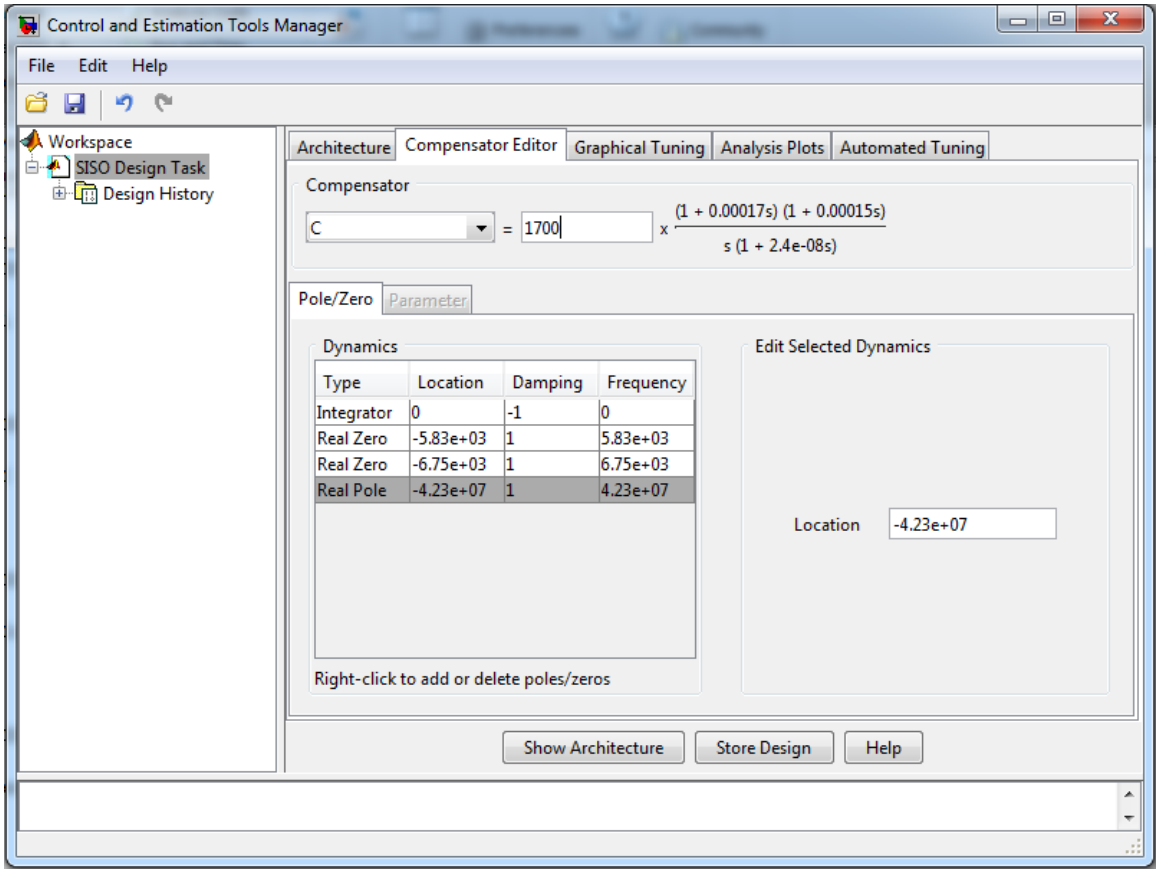

Figure 5.1. Using Matlab's™ Sisotool™ to derive a compensator based on real boost converter plant component values and fuel cell impedance model. The compensator H(s) shown in Figure 5.1 is here labeled "C".

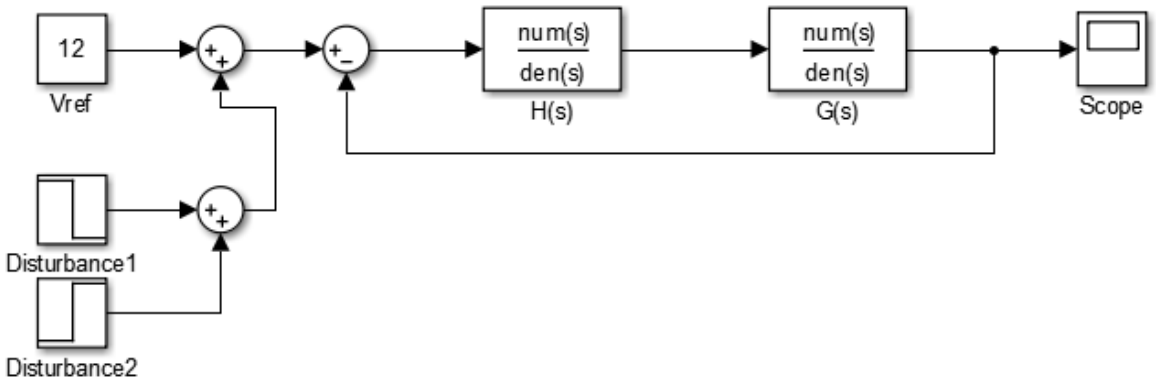

Figure 5.2. Simulink block diagram to test the linear control system design of voltage mode control for the DBFC converter system.

The results in Figure 5.3 show the system tracks voltage references with zero steady state error. Changes in reference produce slight overshoot which does not seem to agree with the proposed $60°$ phase margin design constraint. However, referring to the loop gain of the system which was originally presented in the bode plot in Figure 4.5 it is observable that the phase margin is $60°$ at the crossover frequency of ~150krad/sec but there is actually a slight sag in phase margin before this region where it is in the approximate range of $50°$ to $60°$. This can account for the slight ~5% overshoot observed in simulation. Furthermore, the final system will include damping elements in many places not included in the model such as the MOSFET on state resistance, output capacitor ESR, track impedances and connector impedances that will serve to further dampen the response to the desired shape. If settling time is defined as the time it takes for the output to permanently stabilize within 10% of the target, then this system only required ~13us to reach 10.8 volts and stay within the range [10.8~13.2] on the initial rising transient. This time is in alignment with the ~150krad/sec bandwidth of the system initially seen in the bode plot. 10% bounds were added to the figure to demonstrate how even with the slight over and undershoots that follow the initial rise the output remains within 10% of the reference voltage.

5.3. Boost converter component selection

In this section the real component values for the boost converter components will be justified. The design specifications for the boost converter are outlined in table 5.2.

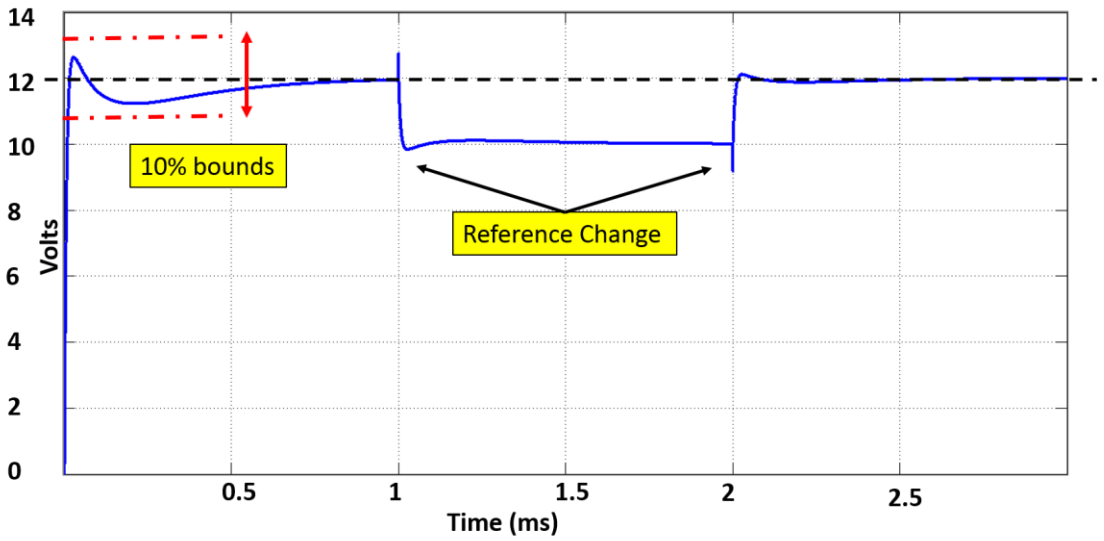

Figure 5.3. Simulink simulation results of the DBFC boost converter system using voltage mode control. The initial reference of 12V is tracked with zero steady state error. Further, the +/- 2V disturbances introduced each millisecond demonstrate the steady state tracking ability and disturbance rejection.

Table 5.2. DBFC system specifications and basic design requirements.

Converter specifications	
Input voltage range	[4~8] volts
Output voltage	12 volts
Operating mode	Continuous conduction mode (CCM)
Nominal Load	6Ω (24 Watts)
Maximum current ripple $\Delta i_{L\,max}$	0.66 Amps
Maximum output voltage ripple Δv_o	50mVolts
Switching frequency f_s	100kHz

The boost converter in this system is being designed to operate in continuous conduction mode (CCM). This means that in steady state at no point within an entire switching period will the inductor current be less than or equal to 0. That condition is known as discontinuous conduction mode or DCM. Designing for CCM allows for useful derivations that can be applied to determine appropriate inductor and capacitor sizing known as the principles of inductor volt-second balance and capacitor charge balance.

The inductor volt-second principles states that the net change in inductor current over one switching period is equal to zero and therefore the integral of the applied inductor voltage over a single switching period is 0. This also means that the rise in inductor current in the first part of a single switching period DT_s is of equal magnitude and opposite sign to what occurs in the second part of the period $D'T_s$. Thus one only needs to consider the switch on time or off time when calculating inductor current ripple magnitude. The individual circuits of a boost converter for the switch in each position was originally introduced in Figures 3.1-3.3 and it is evident that when neglecting DBFC impedance the applied voltage across the inductor was simply as in (5.3):

$$V_L = V_g \tag{5.3}$$

If the current ripple Δi_L is defined as the magnitude the current rises above or falls below the *average* DC current value, then the total peak-to-peak ripple is $2\Delta i_L$. Using these relationships (5.4) can be derived which represents the total current rise within the on-time of the switching interval. Subsequently (5.5) can be derived where T_s was replaced with $\frac{1}{f_s}$ and solved for L. Since the maximum ripple specification was 0.66 A, L is found to be 15uH which is the value used this design.

$$2\Delta i_L = \frac{di_L}{dt} DT_s = \frac{V_g}{L} DT_s \tag{5.4}$$

$$L = \frac{DV_g}{f_s 2\Delta i_L} \tag{5.5}$$

The principle of capacitor charge balance means that the net change over one switching period of the capacitor voltage must be zero, so in equilibrium the integral of the capacitor current over one switching period should be zero [23]. Using a similar

approach as with inductor volt-second balance the charge balance equation can be found to be as in (5.6) where Δv_o is the output voltage ripple and I_o is the average or DC output load current. Using the maximum ripple specification of 50mVolts the output capacitor value chosen is 100uF.

$$C_o = \frac{DI_o}{f_s 2\Delta v_o} \tag{5.6}$$

5.4. Power consumption and supercapacitor selection

Before calculating the supercapacitor value according to (4.7), the variables t_Δ and P_{pump} were optimized to achieve the minimum energy consumption, or the minimum of $t_\Delta * P_{pump}$. Firstly, 4 flow rate speeds were applied to both the anode and cathode sides of the fuel cell and the resulting time to reach 8 Volts under no load conditions was measured. This resulted in the matrix of values depicted in Figure 5.4.

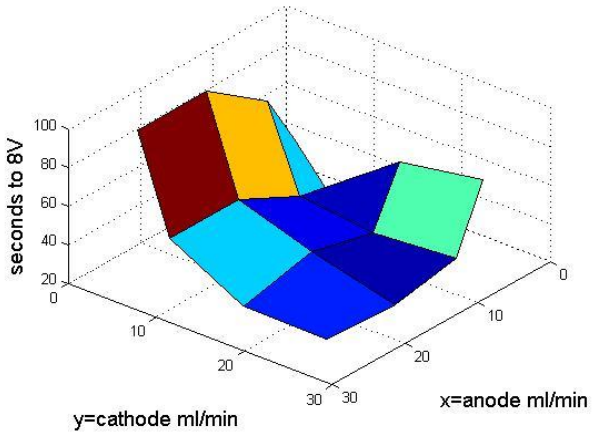

Figure 5.4. Surface visualizing the time for the fuel to reach 8 Volts from 0 Volts with variable anode and cathode fuel flow rates. (t_Δ)

Next, the power consumption of the pumps for each of the 4 flow rates was measured. To calculate the total energy consumed in each of the scenarios in Figure 5.4

each point was multiplied by the power consumption of both pumps, as in (5.7). This resulted in the matrix of values shown in Figure 5.5.

$$Energy = t_{\Delta}(P_{pump,anode} + P_{pump,cathode}) \tag{5.7}$$

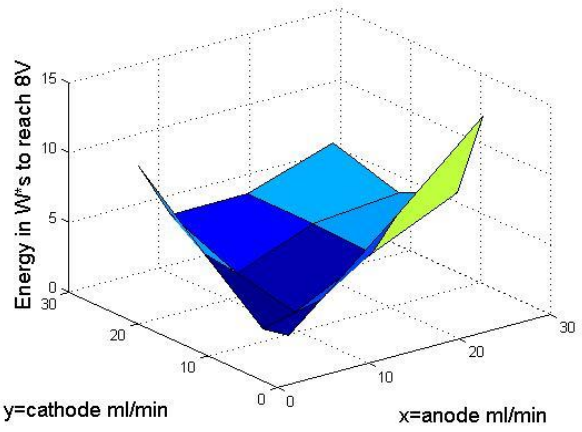

Figure 5.5. Surface visualizeing energy consumption ($t_{\Delta} * P_{Pumps}$)

In general, faster pump speeds during startup resulted in larger power consumption P_{pump} and in smaller voltage start up time t_{Δ}. Finding the minimal value of the pump energy consumption during startup resulted in the following values of $t_{\Delta} = 31s$ and $P_{pumps} = \left(P_{pump,anode} + P_{pump,cathode}\right) \cong 0.55W$. A plot of the fuel cell voltage during startup under these optimum flow rate conditions is shown in Figure 5.6.

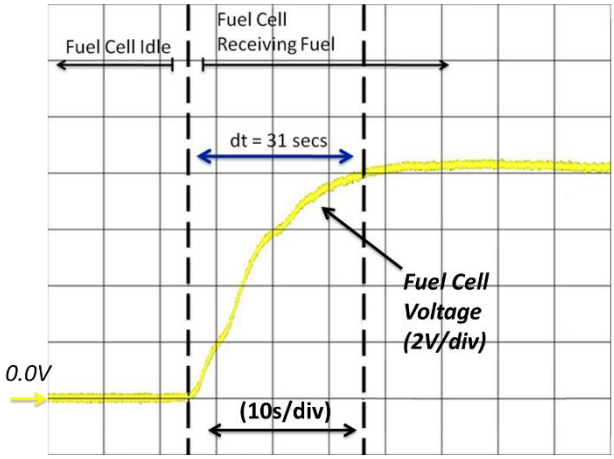

Figure 5.6. Energy optimal fuel cell start-up voltage transient

The last values required to be found for determining a minimum supercapacitor value are the efficiencies η_1 and η_2. The efficiency of the boost converter was tested and found to be approximately 90% at rated conditions, hence $\eta_1 = 0.9$. Furthermore, Figure 5.7 shows the experimentally observed discharge time of 4 series connected supercapacitors. This discharge curve was fitted and found to closely resemble an exponentially decaying signal with an asymptote at 10V as described by (5.8) where t is in hours. Therefore, a conservative value of η_2 can be chosen to be the approximate long-term charge percentage taking into account decay, or $\eta_2 = {}^{10}/_{12} \cong 0.8333$.

$$\eta_2 \cong 10 + 2e^{-0.05t} \tag{5.8}$$

Finally, the minimum supercapacitor value can be calculated and the result is shown in (5.9). Because supercapacitor technology continues to improve, a component was found that met size, weight, and reasonable cost requirements that far exceeded this minimum value. Four Taiyo Yuden PAS1220LA3R0905 3V, 9F were placed in series to achieve an equivalent 12V, 2.25F supercapacitor.

$$C_s \geq \frac{2t_\Delta(P_{elec}+P_{pump})}{(V^2)\eta_1\eta_2} = \frac{2*31*(0.5)}{(10^2)*0.9*0.8333} \cong 0.44F \quad (5.9)$$

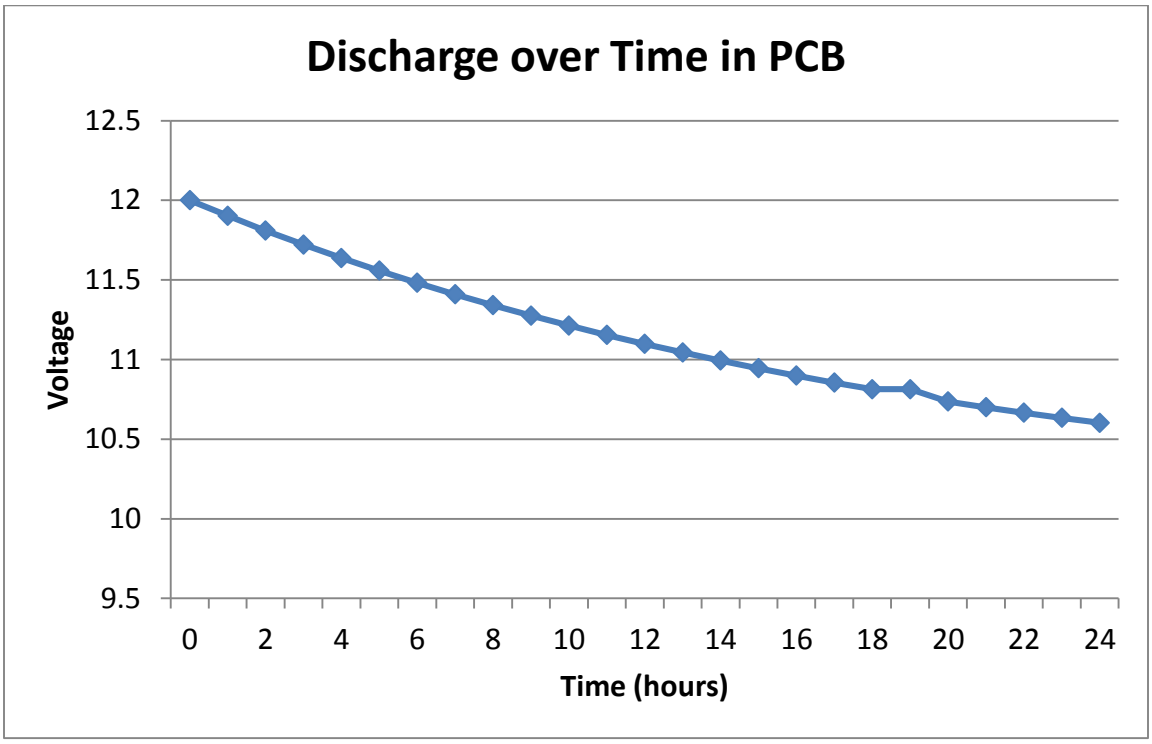

Figure 5.7. Experimentally observed discharge rate of series connected Taiyo Yuden PAS1220LA3R0905 supercapacitors charge to their rated voltage. The discharge can be approximately described by (7.6).

5.5. Fuel cell and boost converter experimental configuration

The experimental setup consists of a 5-cell direct borohydride fuel cell, two containers containing the anode and cathode fuels, tubing to connect the fuel to the fuel cell, two pumps (KNF CH-6210-Sursee, 0.4W) to circulate the anode and cathode fuels to the fuel cell. The fuel is recycled into its respective container and thus the byproducts of the fuel cell chemical reaction continuously mix and/or dilute the fuel solutions over time. The boost converter consists of a 4-layer printed circuit board (PCB) containing a TI DSP (TMS320F28035) controller, the main power stage components, motor drivers,

supercapacitors and loads. This converter was designed to the specifications originally listed in table 5.2.

This experiment is based on the test results of the DBFC research group at the Center for Clean Energy Engineering at the University of Connecticut. They optimized fuel and oxidant concentrations for maximum power output and they found that maximum power output was obtained using an anode fuel containing 5 wt% $NaBH_4$ in 10 wt% NaOH and a cathode fuel containing 15 wt% H_2O_2 in 1.5M H_2SO_4. Meanwhile, using a higher concentration of either sodium borohydride or sodium hydroxide will increase the longevity of the fuel (smaller than 10 wt% and 20 wt% respectively). The 5-cell DBFC has 45cm^2 active area per cell and the MEA (membrane electrode assembly) for each of the 5 cells consisted of a Nafion-117 membrane (pressed at 125^{0}C and 60kg/cm^2) with Pt/C anode catalyst and Au/C cathode catalyst [11]. Figure 5.8 shows the overall DBFC test setup while Figure 5.9 shows a close up of the top-side of the DC-DC converter PCB.

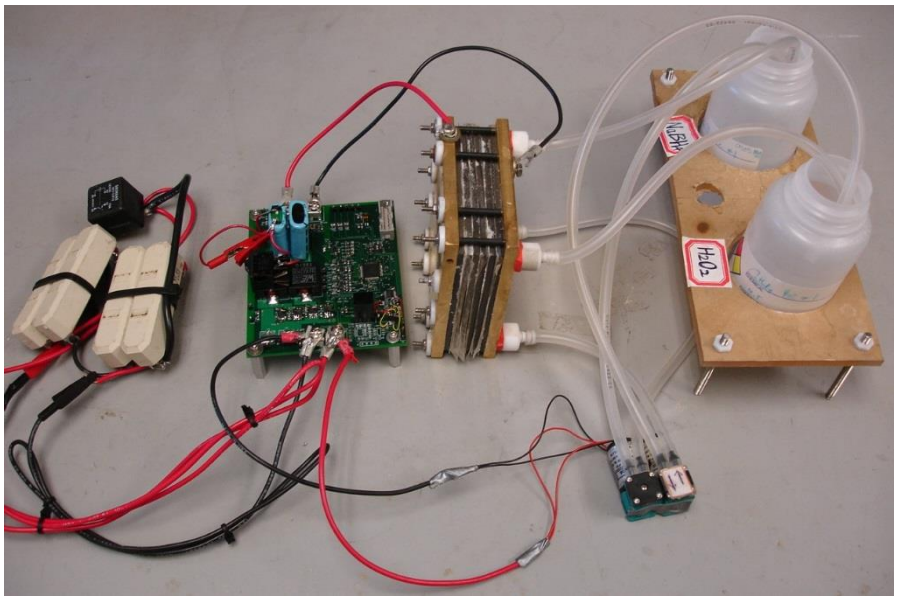

Figure 5.8. DBFC system test setup.

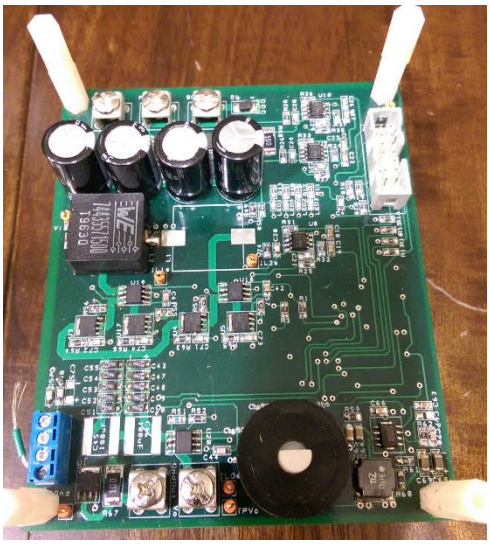

Figure 5.9. Top side of 4-layer DBFC boost converter printed circuit board.

5.6. Experimental procedure and results analysis

Firstly, in order to obtain a dc model of our fuel cell the V-I characteristics were measured.

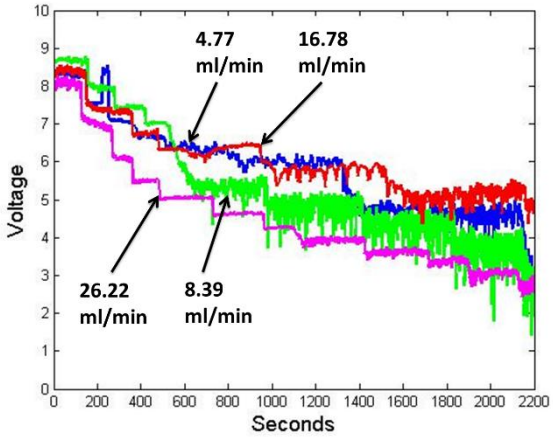

Figure 5.10. V-I characteristics of DBFC with varying flow rates.

In Figure 5.10, four V-I characteristics were obtained with varying flow rates. For each data set, the anode and cathode were simultaneously run at either 4.77mL/min, 8.39mL/min, 16.78mL/min, or 26.22mL/min. Based on the data in Figure 5.10 a linear fit

can be used to construct a dc model of the fuel cell power supply source as a series voltage source and resistance as first explained in section 2.2. This model is sufficient for the purposes of this paper, and an equivalent circuit using the flow rate of 26.22mL/min can be seen in Figure 5.11.

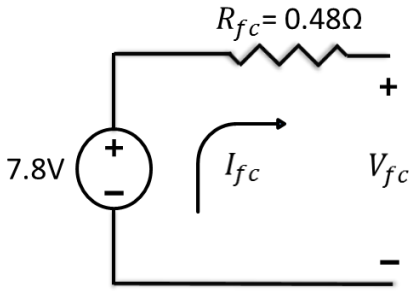

Figure 5.11. Fuel Cell Source Model based on VI curve statistics

Initially, an external power supply was used to charge the supercapacitor bank to 10 Volts. The control reference is set to 10 Volts, and connecting an external power supply to the output of the converter automatically initiates charge mode. A plot of the supercapacitor voltage and the MOSFET switch voltage (only active during the buck charging operation) are presented in Figure 5.12.

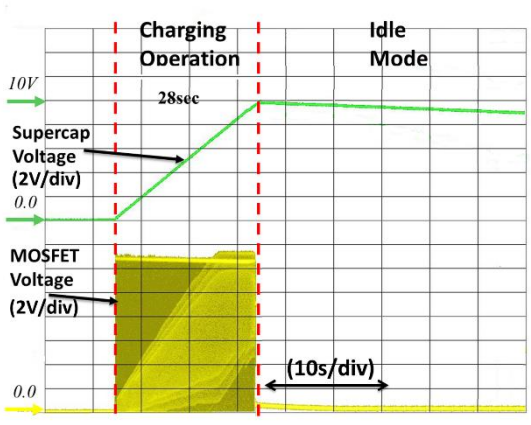

Figure 5.12. Supercapacitor charging where the synchronously switched boost converter acts as a buck converter with a charging voltage source connected to the output of the converter.

The system can then rest at this stage until the charging source is removed from the output, the desired load is connected, and a switch or other mechanism such as a digital message via a serial communication link indicates to the board system start up. At this point, the converter acts as a boost converter using the supercapacitors to run both the power electronics and pumps in order to begin producing fuel cell voltage. A plot of the converter input (supercapacitor) voltage and converter output voltage during this turn on stage can be seen in Figure 5.13. The first region in Figure 5.13 is idle mode, where the capacitors are holding their charge and no operation required. In the second region, start-up operation is taking place and the supercapacitors are discharging. Because of the high side diodes on the converter legs, the supercapacitor voltage is reflected at the output in this region. In the third and final region, the converter has begun normal boost-mode operation. The input voltage begins to level as the fuel begins producing power. Also, the output is immediately regulated to 12V. Once the fuel cell reaches this self-sustainable voltage level, in will operate under voltage controlled boost operation mode as long as the system remains on and there is adequate fuel supply.

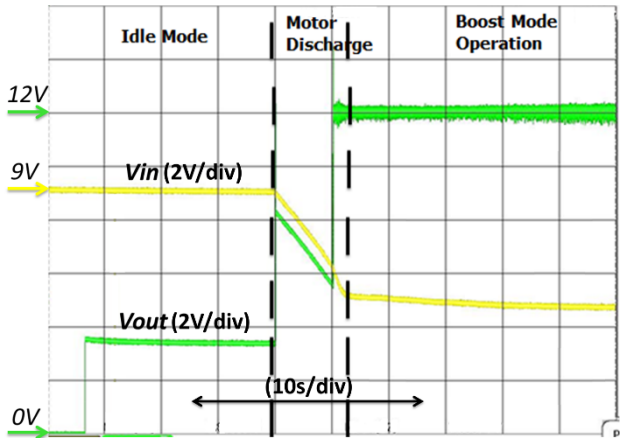

Figure 5.13. Input voltage and converter output voltage of the DBFC system during startup

Lastly, converter dynamics were tested. In Figure 5.14 both the output current and output voltage are plotted. First, the load is increased from approximately 1A to 2A 0.4 seconds into the window, then back from 2A to 1A 1.6 seconds into the window. The output voltage stabilizes to 12 volts in both cases in approximately 10 milliseconds. This scenario can be considered a disturbance and is not a step change in voltage reference as was previously studied, so a 10 millisecond response time to a disturbance is reasonable for the modeling previously done also taking into account and non-idealities of the circuit that were not included in the original models.

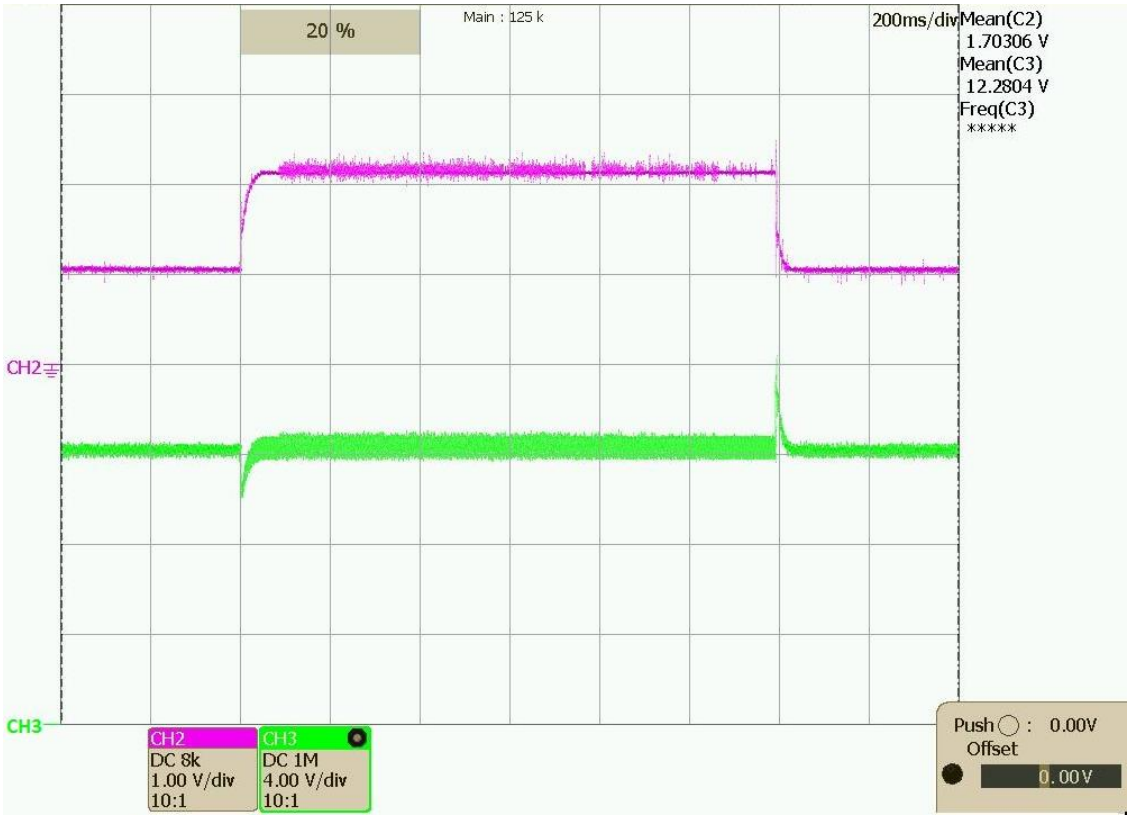

Figure 5.14. Load disturbance test while the DBFC converter is operating in voltage control mode. The upper trace is load current with 1 Amp/division scaling, so the load was increased from 1 Amp to 2 Amps and then back to 1 Amp. The lower trace is output voltage which was regulating to 12 Volts and shows transients during each load disturbance event before eventually settling to 12 Volts again.

Conclusion

A direct-borohydride fuel cell and power electronics converter for portable applications has been presented in this thesis. The system consists of a fuel cell, a digitally controlled boost converter, supercapacitors, and fuel cell balance of system components such as pumps and fuel containers. The system demonstrated several benefits including the improved energy density of direct-borohydride fuel cells over more common hydrogen or hydrocarbon proton-exchange membrane fuel cells, a custom boost converter tailored to the electro-chemical properties of the fuel cell, and supercapacitors which have the dual advantage of improved converter dynamic response an energy storage for remote startup eliminating the need for batteries.

The properties, benefits and drawbacks of this particular classification of fuel cell were presented. The electro-chemical reactions of the DBFC were presented and its steady state operating conditions experimentally verified via voltage-current (V-I) curve characterization. Furthermore, in order to obtain a dynamic electrical model of the fuel cell for control purposes electrochemical impedance spectroscopy was performed.

The DBFC presented in this thesis produces an output voltage in the range of [4~8] volts based on load and environmental conditions. To produce a consistent voltage useful to portable electronics a non-isolated boost converter topology was chosen. This topology allows for a well regulated 12V output which is useful to many portable electronic devices and can be combined with off the shelf buck or flyback converters if 5V, 3.3V and other supply voltages are required. Furthermore, this topology facilitates

commercially available supercapacitors at the fuel cell side of the converter. The supercapacitors were shown to negate parasitic capacitances and impedances of the fuel cell and allow for a higher bandwidth boost converter controller and better output regulation. Furthermore, without any additional hardware these supercapacitors were charged in a controlled manner when an external supply was connected to the output of the converter. This “pre-charge” can store enough energy to operate the fuel cell pumps long enough to remotely start the system without the need for additional energy storage such as batteries or the converters required to interface them, simplifying the system and reducing costs.

A generic state-space modeling method was presented to create various transfer functions for converters. This approach was applied to the boost converter used in the system with varying levels parasitic modeling included in the model. The simplest model that still captured the significant dynamics of the converter transfer function was derived and presented. This plant transfer function in combination with the linearized fuel cell model derived from electrochemical impedance spectroscopy was used to create a custom controller in Matlab™. A pole-placement method was used to achieve a gain margin of 10.3dB at 4.05e+06 radians/sec and a phase margin of 66.8° at 1.3e+05 radians/sec. This was shown to be more than what was achievable in the absence of the additional supercapacitors at the input of the boost converter.

A 24W prototype converter was designed and implemented in hardware. This system successfully demonstrated the key principles of this system. First, the

supercapacitors were charged to near their rated voltage using an external power supply. This process took approximately 30 seconds. These supercapacitors were left in circuit to discharge and their self-discharge rate was noted. More than 24 hours later, the charge remaining in the supercapacitors was enough to run the digitally controlled boost converter and run the 12V fuel cell pumps long enough for the fuel cell to begin producing power. The system then ran with regulated output voltage as long as sufficient fuel supply was present. Output voltage load transients were introduced and the converter transient response was seen to align with the theoretically designed compensator. In choosing supercapacitors, energy storage was the more difficult requirement than the value required to negate the dynamic effects of the DBFC. Test waveforms have been provided for the operation modes of this system: charging, start up, normal operation, and response to external disturbance.

References

[1] M. W. Ellis, M. R. Von Spakovsky, and D. J. Nelson, "Fuel cell systems: efficient, flexible energy conversion for the 21st Century," Proc. IEEE, vol. 89, issue 12, pp. 1808–1818, 2001

[2] Fuel Cell Systems Explained second edition, James Larminie, Andrew Dicks, John Wiley and sons 2003.

[3] A. Kirubakaran, S. Jain and R.K. Nema, "A review on fuel cell technologies and power electronic interface," Renew. Sustain Energy Rev, vol. 13, pp. 2430–2440, 2009.

[4] EG&G Technical Services. "Fuel Cell Handbook (seventh edition)." U.S. Department of Energy, Office of Fossil Energy, Nov. 2004.

[5] L. Carrette, K.A. Friedrich and U. Stimming. "Fuel Cells – Fundamentals and Applications." Vol. 1, pp. 5-39, May 2001.

[6] A. Leo. "Stationary Fuel Cell Power Systems with Direct FuelCell Technology Tackle Growing Distributed Baseload Power Challenge." Internet: http://www.fuelcellenergy.com/assets/Fuel-Cell-Technology-White-Paper1.pdf, [Apr. 1st, 2015]

[7] NASA. "Summary: Space Applications of Hydrogen and Fuel Cells." Internet: http://www.nasa.gov/topics/technology/hydrogen/hydrogen_2009.html, [Mar. 15th, 2015]

[8] T. Koehler. "A Green Machine." Internet: http://www.boeing.com/news/frontiers/archive/2008/may/ts_sf04.pdf, [Mar. 15th, 2015]

[9] P. Robinson. "Underwater Applications." Internet: http://www.protonex.com/solutions/underwater-applications/, [Mar. 15th, 2015]

[10] J. Ma, N. A.Choudhury, Y. Sahai, "A comprehensive review of direct borohydride fuel cells," Renew Sust Energ Rev, 14, pp. 183–199, 2010.

[11] X. Zhu. "Design and Analysis of a Direct Borohydride Fuel Cell DC-DC Converter for Portable Applications." M.Sc. Thesis, University of Connecticut, United States, 2010.

[12] Z.P. Li, B.H. Liu, K. Arai, and S. Suda, "Development of the direct borohydride fuel cell," J. Alloys Compd, vol. 404–406, pp. 648–652, 2005.

[13] A.M. Karim, J.A. Federici, D.G. Vlachos, "Portable power production from methanol in an integrated thermoeletric/microreactor system," J. Power Sources, 179, pp. 113-120, 2008

[14] B.H. Liu and Z.P. Li, "Current status and progress of direct borohydride fuel cell technology development," J. Power Sources, vol. 187, pp. 291–297, 2009.

[15] S. Towne, M. Carella, W.E. Mustain, V. Viswanathan, P. Rieke, U. Passaogullari, P. Singh. "Performance of a Direct Borohydride Fuel Cell." *The Electrochemical Society Transaction,* vol. 25, pp. 1-7, 2009. (referenced in para 1 of 1.6)

[16] G. Maggio, V. Recupero and L. pino, "Modeling polymer electrolyte fuel cells: an innovative approach," J. Power Source, vol. 101, pp. 275–286, 2001.

[17] M D. Lukas, K. Y. Lee and H. Ghezel-Ayagh, "An explicit dynamic model for direct reforming carbonate fuel cell stack," IEEE Trans Energy Conver, vol. 16, no. 3, Sep. 2001.

[18] J.C. Amphlett, R.F. Mann, B.A. Peppley, P.R. Roberge, and A. Rodrigues, "A practical PEM Fuel cell Model for simulation vehicle power sources," Proceedings of the Battery Conference on Applications and Advantages, pp. 221–226, 1995.

[19] W. Choi, J.W. Howze and P. Enjeti, "Development of an equivalent circuit model of a fuel cell to evaluate the effects of inverter ripple current," J. Power Sources, vol. 158, pp. 1324–1332, 2006.

[20] B.H. Liu, Z.P. Li, K. Arai, S. Suda. "Performance improvement of a micro borohydrude fuel cell operating at ambient conditions." *Electrochemica Acta,* vol. 50, pp. 3719-3725, Feb. 2005.

[21] X. Yuan, H. Wang. *PEM fuel cell electrocatalysts and Catalyst Layers, fundamentals and applications*, London: Springer-Verlag, 2008

[22] V. Ramani, J.M.Fenton and H.R.Kunz, "Experimental methods and data analyses for polymer electrolyte fuel cells," Scribner Associates, Inc. 2005.

[23] R. W. Erickson and D. Maksimovic, "Fundamentals of power electronics second edition," New York, NY: Springer Science Business Media, 2001.

APENDIX I: Derivation of average state space model for interleaved (3-state) boost converter

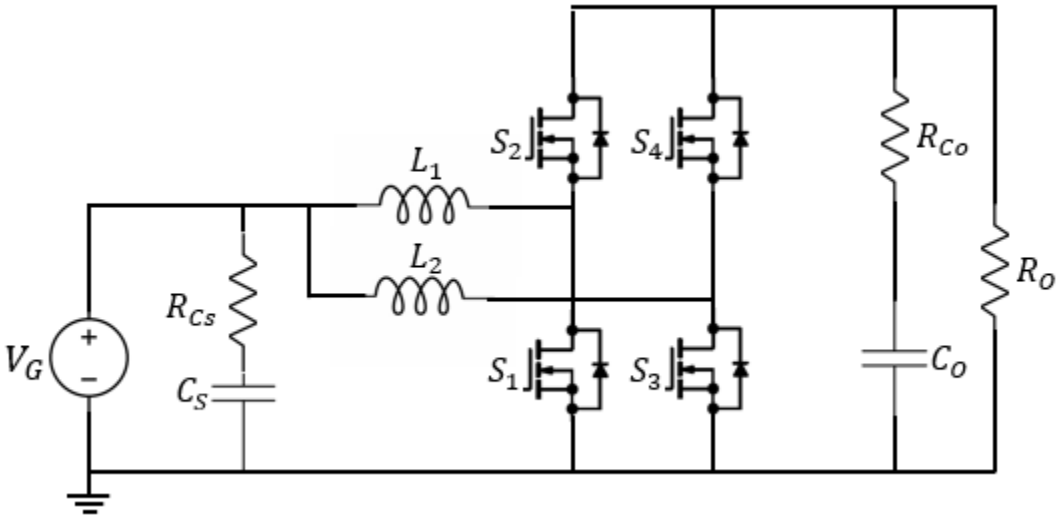

Figure App.1. Interleaved non-ideal switching boost converter. This circuit contains ESR for both the input and output capacitors, and when and of the switches S1-S4 are on their "on-state" resistance is modeled by the variable R_{DSon}.

Position 1 Equations:

$$C_{sc}\dot{V_{sc}} = \frac{V_G - V_{sc}}{R_{Csc}} = \frac{1}{R_{Csc}}V_G - \frac{1}{R_{Csc}}V_{sc} \quad \text{(A1)}$$

$$C_o\dot{V_{co}} = i_{L2} - i_o = i_{L2} - \frac{V_o}{R_L} \quad \text{(A2)}$$

However:

$$V_o = \frac{R_L}{R_{co}+R_L}(V_{co} + R_{co}i_{L2}) \quad \text{(A3)}$$

Therefore:

$$C_o\dot{V_{co}} = i_{L2} - \frac{1}{R_{co}+R_L}(V_{co} + R_{co}i_{L2}) = i_{L2}\left(1 - \frac{R_{co}}{R_{co}+R_L}\right) - V_{co}\left(\frac{1}{R_{co}+R_L}\right) \quad \text{(A4)}$$

$$L_1\dot{\imath_{L1}} = V_G - R_{DSon} * i_{L1} \quad \text{(A5)}$$

$$L_2 \dot{i_{L2}} = V_G - R_{DSon} * i_{L2} - V_o = V_G - R_{DSon} * i_{L2} -$$

$$\frac{R_L}{R_{co}+R_L}(V_{co} + R_{co} i_{L2}) = V_G + i_{L2}\left(-R_{DSon} - \frac{R_L R_{co}}{R_L+R_{co}}\right) - V_{co}\left(\frac{R_L}{R_{co}+R_L}\right) \quad \text{(A6)}$$

$$I_G = -\frac{V_{SC}}{R_{Csc}} + i_{L1} + i_{L2} + \frac{V_G}{R_{Csc}} \quad \text{(A7)}$$

$$\begin{bmatrix} C_{sc} & 0 & 0 & 0 \\ 0 & C_o & 0 & 0 \\ 0 & 0 & L_1 & 0 \\ 0 & 0 & 0 & L_2 \end{bmatrix} \begin{bmatrix} \dot{V_{sc}} \\ \dot{V_{co}} \\ \dot{i_{L1}} \\ \dot{i_{L2}} \end{bmatrix} =$$

$$\begin{bmatrix} -\frac{1}{R_{Csc}} & 0 & 0 & 0 \\ 0 & -\frac{1}{R_{co}+R_L} & 0 & 1-\frac{R_{co}}{R_{co}+R_L} \\ 0 & 0 & -R_{DSon} & 0 \\ 0 & -\frac{R_L}{R_{co}+R_L} & 0 & -R_{DSon} - \frac{R_L R_{co}}{R_L+R_{co}} \end{bmatrix} \begin{bmatrix} V_{sc} \\ V_{co} \\ i_{L1} \\ i_{L2} \end{bmatrix} + \begin{bmatrix} \frac{1}{R_{Csc}} \\ 0 \\ 1 \\ 1 \end{bmatrix} V_G \quad \text{(A8)}$$

$$I_G = \begin{bmatrix} -\frac{1}{R_{Csc}} & 0 & 1 & 1 \end{bmatrix} \begin{bmatrix} V_{sc} \\ V_{co} \\ i_{L1} \\ i_{L2} \end{bmatrix} + \begin{bmatrix} \frac{1}{R_{Csc}} \end{bmatrix} V_G \quad \text{(A9)}$$

Position 2 Equations:

$$C_{sc} \dot{V_{sc}} = I_G - i_{L1} - i_{L2} \quad \text{(A10)}$$

$$C_o \dot{V_{co}} = i_{L1} - i_o = i_{L1} - \frac{V_o}{R_L} \quad \text{(A11)}$$

However:

$$V_o = \frac{R_L}{R_{co}+R_L}(V_{co} + R_{co} i_{L1}) \quad \text{(A12)}$$

Therefore:

$$C_o \dot{V_{co}} = i_{L1} - \frac{1}{R_{co}+R_L}(V_{co} + R_{co} i_{L1}) = i_{L1}\left(1 - \frac{R_{co}}{R_{co}+R_L}\right) -$$

$$V_{co}\left(\frac{1}{R_{co}+R_L}\right) \quad \text{(A13)}$$

$$L_1 \dot{\imath_{L1}} = V_G - R_{DSon} * i_{L1} - V_o = V_G - R_{DSon} * i_{L1} - \frac{R_L}{R_{co}+R_L}(V_{co} +$$

$$R_{co} i_{L1}) = V_G + i_{L1}\left(-R_{DSon} - \frac{R_L R_{co}}{R_L+R_{co}}\right) - V_{co}\left(\frac{R_L}{R_{co}+R_L}\right) \quad \text{(A14)}$$

$$L_2 \dot{\imath_{L2}} = V_G - R_{DSon} * i_{L2} \quad \text{(A15)}$$

$$I_G = -\frac{V_{SC}}{R_{Csc}} + i_{L1} + i_{L2} + \frac{V_G}{R_{Csc}} \quad \text{(A16)}$$

$$\begin{bmatrix} C_{sc} & 0 & 0 & 0 \\ 0 & C_o & 0 & 0 \\ 0 & 0 & L_1 & 0 \\ 0 & 0 & 0 & L_2 \end{bmatrix} \begin{bmatrix} \dot{V_{sc}} \\ \dot{V_{co}} \\ \dot{i_{L1}} \\ \dot{i_{L2}} \end{bmatrix} =$$

$$\begin{bmatrix} -\frac{1}{R_{Csc}} & 0 & 0 & 0 \\ 0 & -\frac{1}{R_{co}+R_L} & 1-\frac{R_{co}}{R_{co}+R_L} & 0 \\ 0 & -\frac{R_L}{R_{co}+R_L} & -R_{DSon} - \frac{R_L R_{co}}{R_L+R_{co}} & 0 \\ 0 & 0 & 0 & -R_{DSon} \end{bmatrix} \begin{bmatrix} V_{sc} \\ V_{co} \\ i_{L1} \\ i_{L2} \end{bmatrix} + \begin{bmatrix} \frac{1}{R_{Csc}} \\ 0 \\ 1 \\ 1 \end{bmatrix} V_G \quad \text{(A17)}$$

$$I_G = \begin{bmatrix} -\frac{1}{R_{Csc}} & 0 & 1 & 1 \end{bmatrix} \begin{bmatrix} V_{sc} \\ V_{co} \\ i_{L1} \\ i_{L2} \end{bmatrix} + \begin{bmatrix} \frac{1}{R_{Csc}} \end{bmatrix} V_G \quad \text{(A18)}$$

Position 3 Equations:

$$C_{sc} \dot{V_{sc}} = I_G - i_{L1} - i_{L2} \quad \text{(A19)}$$

$$C_o \dot{V_{co}} = i_{L1} + i_{L2} - i_o = i_{L1} + i_{L2} - \frac{V_o}{R_L} \quad \text{(A20)}$$

However:

$$V_o = \frac{R_L}{R_{co}+R_L}\left(V_{co} + R_{co}(i_{L1} + i_{L2})\right) \quad \text{(A21)}$$

Therefore:

$$C_o \dot{V_{co}} = i_{L1} + i_{L2} - \frac{1}{R_{co}+R_L}\left(V_{co} + R_{co}(i_{L1} + i_{L2})\right) = i_{L1}\left(1 -$$

$$\frac{R_{co}}{R_{co}+R_L}\right) + i_{L2}\left(1 - \frac{R_{co}}{R_{co}+R_L}\right) - V_{co}\left(\frac{1}{R_{co}+R_L}\right) \quad \text{(A22)}$$

$$L_1\dot{\imath_{L1}} = V_G - R_{DSon} * i_{L1} - V_o = V_G - R_{DSon} * i_{L1} - \frac{R_L}{R_{co}+R_L}\left(V_{co} + R_{co}(i_{L1} + i_{L2})\right) = V_G + i_{L1}\left(-R_{DSon} - \frac{R_L R_{co}}{R_L+R_{co}}\right) + i_{L2}\left(-\frac{R_L R_{co}}{R_L+R_{co}}\right) + V_{co}\left(-\frac{R_L}{R_{co}+R_L}\right) \quad \text{(A23)}$$

$$L_2\dot{\imath_{L2}} = V_G - R_{DSon} * i_{L2} - V_o = V_G - R_{DSon} * i_{L2} - \frac{R_L}{R_{co}+R_L}\left(V_{co} + R_{co}(i_{L1} + i_{L2})\right) = V_G + i_{L2}\left(-R_{DSon} - \frac{R_L R_{co}}{R_L+R_{co}}\right) + i_{L1}\left(-\frac{R_L R_{co}}{R_L+R_{co}}\right) - V_{co}\left(\frac{R_L}{R_{co}+R_L}\right) \quad \text{(A24)}$$

$$I_G = \begin{bmatrix} -\frac{1}{R_{Csc}} & 0 & 1 & 1 \end{bmatrix} \begin{bmatrix} V_{sc} \\ V_{co} \\ i_{L1} \\ i_{L2} \end{bmatrix} + \begin{bmatrix} \frac{1}{R_{Csc}} \end{bmatrix} V_G \quad \text{(A25)}$$

$$\begin{bmatrix} C_{sc} & 0 & 0 & 0 \\ 0 & C_o & 0 & 0 \\ 0 & 0 & L_1 & 0 \\ 0 & 0 & 0 & L_2 \end{bmatrix} \begin{bmatrix} \dot{V_{sc}} \\ \dot{V_{co}} \\ \dot{\imath_{L1}} \\ \dot{\imath_{L2}} \end{bmatrix} =$$

$$\begin{bmatrix} -\frac{1}{R_{Csc}} & 0 & 0 & 0 \\ 0 & -\frac{1}{R_{co}+R_L} & 0 & 1-\frac{R_{co}}{R_{co}+R_L} \\ 0 & 0 & -R_{DSon} & 0 \\ 0 & -\frac{R_L}{R_{co}+R_L} & 0 & -R_{DSon} - \frac{R_L R_{co}}{R_L+R_{co}} \end{bmatrix} \begin{bmatrix} V_{sc} \\ V_{co} \\ i_{L1} \\ i_{L2} \end{bmatrix} + \begin{bmatrix} \frac{1}{R_{Csc}} \\ 0 \\ 1 \\ 1 \end{bmatrix} V_G \quad \text{(A26)}$$

$$I_G = \begin{bmatrix} -\frac{1}{R_{Csc}} & 0 & 1 & 1 \end{bmatrix} \begin{bmatrix} V_{sc} \\ V_{co} \\ i_{L1} \\ i_{L2} \end{bmatrix} + \begin{bmatrix} \frac{1}{R_{Csc}} \end{bmatrix} V_G \quad \text{(A27)}$$

Now that the state-space matrices for each switching interval have been derived, the derivation to use them to develop transfer functions is presented next. In the first subinterval of an interleaved switching converter (one switch on and other switch off), the states change as

$$\frac{dx(t)}{dt} = k^{-1}(A_1 < x(t)_{Ts} > + B_1 < u(t)_{Ts} >) \quad \text{(A28)}$$

Therefore the value of the system states at the end of the first subinterval can be expressed as

$$final\ value = initial\ value + (interval\ length * slope) =$$

$$x(dT_S) = x(0) + (dT_s)k^{-1}(A_1 < x(t)_{Ts} > + B_1 < u(t)_{Ts} >) \quad \text{(A29)}$$

Note the above only applies when d < 0.5, otherwise dT_s needs to be replaced by d'T_s. Similarly, in the second subinterval the system states change as

$$\frac{dx(t)}{dt} = k^{-1}(A_2 < x(t)_{Ts} > + B_2 < u(t)_{Ts} >) \quad \text{(A30)}$$

Thus the state vector at the end of subinterval 2 is

$$x\big((1-d)T_s\big) = x(dT_s) + (1-2d)T_s k^{-1}(A_2 < x(t) >_{Ts} + B_2 < u(t) >_{Ts}) \quad \text{(A31)}$$

Finally, the state vector at the end of the switching period can be expressed as

$$x(T_s) = x\big((1-d)T_s\big) + (dT_s)k^{-1}(A_3 < x(t) > T_s + B_3 < u(t) > T_s) \quad \text{(A32)}$$

Substituting A31 into A32 yields

$$x(T_s) = x(dT_s) + (1-2d)T_s k^{-1}(A_2 < x(t) >_{Ts} + B_2 < u(t) >_{Ts}) + (dT_s)k^{-1}(A_3 < x(t) > T_s + B_3 < u(t) > T_s) \quad \text{(A33)}$$

Substituting (A28) into (A33) further yields

$$x(T_s) = x(0) + (dT_s)k^{-1}(A_1 < x(t)_{Ts} > + B_1 < u(t)_{Ts} >) + (1-2d)T_s k^{-1}(A_2 < x(t) >_{Ts} + B_2 < u(t) >_{Ts}) + (dT_s)k^{-1}(A_3 < x(t) >_{Ts} + B_3 < u(t) >_{Ts}) \quad \text{(A34)}$$

Rearranging terms yields

$$x(T_s) = x(0) + T_s k^{-1}(dA_1 + (1-2d)A_2 + dA_3) < x(t) >_{Ts} + T_s k^{-1}(dB_1 + (1-2d)B_2 + dB_3) < u(t) >_{Ts} \quad \text{(A35)}$$

In this average model, the derivative of $< x(t) >_{Ts}$ for one switching period can be approximated as

$$\frac{d < x(t) >_{Ts}}{dt} \cong \frac{x(T_s) - x(0)}{T_s} \quad \text{(A36)}$$

In (A35) it can be seen that subtracting $x(0)$ from both sides of the equation and then dividing both sides by T_s puts the equation in the form of (A36). From there, left-multiplying both sides of the equation by k yields

$$k\frac{d < x(t) >_{Ts}}{dt} = (dA_1 + (1-2d)A_2 + dA_3) < x(t) >_{Ts} + (dB_1 + (1-2d)B_2 + dB_3) < u(t) >_{Ts} \quad \text{(A37)}$$

This is in the form of $k\dot{x} = Ax + Bu$, same arguments above apply to y, so these equations can be used to solve for 0 = AX+BU, Y = CX + EU, i.e. x = A^-1BU, Y = CA^-1BU + EU. To create a linearized model around this average operating point, the following equations that represent perturbations around the quiescent operating point can be used:

$$< x(t) >_{Ts} = X + \hat{x}(t) \quad \text{(A38)}$$

$$< u(t) >_{Ts} = U + \hat{u}(t) \quad \text{(A39)}$$

$$< y(t) >_{Ts} = Y + \hat{y}(t) \quad \text{(A40)}$$

$$d(t) = D + \hat{d}(t), d'(t) = D' + \hat{d}'(t) \quad \text{(A41)}$$

Substituting these into A37 results in

$$k\frac{d(X+\hat{x}(t))_{Ts}}{dt} = \left(\left(D + \hat{d}(t)\right)A_1 + \left(1 - 2\left(D + \hat{d}(t)\right)\right)A_2 + \left(D + \hat{d}(t)\right)A_3\right)\left(X + \hat{x}(t)\right)_{Ts} +$$

$$\left(\left(D + \hat{d}(t)\right)B_1 + \left(1 - 2\left(D + \hat{d}(t)\right)\right)B_2 + \left(D + \hat{d}(t)\right)B_3\right)\left(U + \hat{u}(t)\right)_{Ts} \quad \text{(A42)}$$

Noting A42 and using the definitions in A43-A7 the can be expressed as in A48.

$$\frac{dX}{dt} = 0 \quad \text{(A43)}$$

$$A = DA_1 + (1 - 2D)A_2 + DA_3 \quad \text{(A44)}$$

$$B = DB_1 + (1 - 2D)B_2 + DB_3 \quad \text{(A45)}$$

$$C = DC_1 + (1 - 2D)C_2 + DC_3 \quad \text{(A46)}$$

$$E = DE_1 + (1 - 2D)E_2 + DE_3 \quad \text{(A47)}$$

$$k\frac{d\hat{x}(t)_{Ts}}{dt} =$$

$$\left[A + \hat{d}(t)(A_1 - 2A_2 + A_3)\right]\left(X + \hat{x}(t)\right) + \left[B + \hat{d}(t)(B_1 - 2B_2 + B_3)\right]\left(U + \hat{u}(t)\right) \quad \text{(A48)}$$

Distributing terms through and cancelling second order terms result in

$$k\frac{d\hat{x}(t)_{Ts}}{dt} = AX + BU + A\hat{x}(t) + B\hat{u}(t) + \hat{d}(t)[(A_1 - 2A_2 + A_3)X + (B_1 - 2B_2 + B_3)U] \quad \text{(A49)}$$

Since by definition the DC term $AX + BU = 0$, the final result is

$$k\frac{d\hat{x}(t)_{Ts}}{dt} = A\hat{x}(t) + B\hat{u}(t) + \hat{d}(t)[(A_1 - 2A_2 + A_3)X + (B_1 - 2B_2 + B_3)U] \quad \text{(A50)}$$

APENDIX II: State-space equations including input and output capacitance ESR and switch on-state resistance

Position 1 Equations:

$$C_{in}\dot{V_{Cin}} = \frac{V_G - V_{Cin}}{R_{Cin}} = \frac{1}{R_{Cin}}V_G - \frac{1}{R_{Cin}}V_{Cin} \quad \text{(A51)}$$

$$C_o\frac{dV_{Co}}{dt} = -\frac{V_o}{R_o} = V_{Co}\left(-\frac{1}{R_{Co}+R_o}\right) \quad \text{(A52)}$$

$$L_1\dot{i_{L1}} = V_G - R_{DSon} * i_{L1} \quad \text{(A53)}$$

$$I_G = I_{Cin} + i_{L1} = \left(\frac{V_G - V_{Cin}}{R_{Cin}}\right) + i_{L1} = \frac{1}{R_{Cin}}V_G - \frac{1}{R_{Cin}}V_{Cin} + i_{L1} \quad \text{(A54)}$$

$$\begin{bmatrix} C_{in} & 0 & 0 \\ 0 & C_o & 0 \\ 0 & 0 & L_1 \end{bmatrix}\begin{bmatrix} \dot{V_{Cin}} \\ \dot{V_{co}} \\ \dot{i_{L1}} \end{bmatrix} = \begin{bmatrix} -\frac{1}{R_{Cin}} & 0 & 0 \\ 0 & -\frac{1}{R_{Co}+R_o} & 0 \\ 0 & 0 & -R_{DSon} \end{bmatrix}\begin{bmatrix} V_{Cin} \\ V_{co} \\ i_{L1} \end{bmatrix} + \begin{bmatrix} \frac{1}{R_{Cin}} \\ 0 \\ 1 \end{bmatrix}V_G \quad \text{(A55)}$$

$$I_G = \begin{bmatrix} -\frac{1}{R_{Cin}} & 0 & 1 \end{bmatrix}\begin{bmatrix} V_{Cin} \\ V_{co} \\ i_{L1} \end{bmatrix} + \begin{bmatrix} \frac{1}{R_{Cin}} \end{bmatrix}V_G \quad \text{(A56)}$$

Position 2 Equations:

$$C_{in}\dot{V_{Cin}} = \frac{V_G - V_{Cin}}{R_{Cin}} = \frac{1}{R_{Cin}}V_G - \frac{1}{R_{Cin}}V_{Cin} \quad \text{(A57)}$$

$$C_o\frac{dV_{Co}}{dt} = i_{L1} - \frac{V_o}{R_o} = i_{L1} - \frac{V_{Co}+V_{Rco}}{R_o} = i_{L1} - \frac{V_{Co}+i_{Co}*R_{Co}}{R_o} \quad \text{(A58)}$$

$$C_o\frac{dV_{Co}}{dt} = i_{Co} \quad \text{(A59)}$$

Because of A59 it is possible to combine terms to obtain

$$C_o\frac{dV_{Co}}{dt} = \frac{R_o}{R_o+R_{Co}}i_{L1} - \frac{1}{R_o+R_{Co}}V_{Co} \quad \text{(A60)}$$

$$L_1\dot{i_{L1}} = V_G - (R_{DSon} * i_{L1}) - (R_{Co} * i_{Co}) - V_{Co} = V_G - (R_{DSon} * i_{L1}) - \left(\frac{R_o * R_{Co}}{R_o+R_{Co}}i_{L1} - \frac{R_{Co}}{R_o+R_{Co}}V_{Co}\right) - V_{Co} = V_G + \left(-\frac{R_o * R_{Co}}{R_o+R_{Co}} - R_{dsON}\right)i_{L1} + \left(\frac{R_{Co}}{R_o+R_{Co}} - 1\right)V_{Co} \quad \text{(A61)}$$

$$I_G = I_{Cin} + i_{L1} = \left(\frac{V_G - V_{Cin}}{R_{Cin}}\right) + i_{L1} = \frac{1}{R_{Cin}} V_G - \frac{1}{R_{Cin}} V_{Cin} + i_{L1} \quad \text{(A62)}$$

$$\begin{bmatrix} C_{in} & 0 & 0 \\ 0 & C_o & 0 \\ 0 & 0 & L_1 \end{bmatrix} \begin{bmatrix} \dot{V_{Cin}} \\ \dot{V_{co}} \\ \dot{\imath_{L1}} \end{bmatrix} = \begin{bmatrix} -\frac{1}{R_{Cin}} & 0 & 0 \\ 0 & -\frac{1}{R_{Co}+R_o} & \frac{R_o}{R_o+R_{Co}} \\ 0 & \frac{R_{Co}}{R_o+R_{Co}} - 1 & -\frac{R_o R_{Co}}{R_o+R_{Co}} - R_{dsON} \end{bmatrix} \begin{bmatrix} V_{Cin} \\ V_{co} \\ i_{L1} \end{bmatrix} + \begin{bmatrix} \frac{1}{R_{Cin}} \\ 0 \\ 1 \end{bmatrix} V_G \quad \text{(A63)}$$

$$I_G = \begin{bmatrix} -\frac{1}{R_{Cin}} & 0 & 1 \end{bmatrix} \begin{bmatrix} V_{Cin} \\ V_{co} \\ i_{L1} \end{bmatrix} + \begin{bmatrix} \frac{1}{R_{Cin}} \end{bmatrix} V_G \quad \text{(A64)}$$